



Evaluation of sea-surface photosynthetically available radiation algorithms under various sky conditions and solar elevations

SRIKANTH AYYALA SOMAYAJULA,^{1,*} EMMANUEL DEVRED,² SIMON BÉLANGER,³ DAVID ANTOINE,^{4,5} V. VELLUCCI,⁴ AND MARCEL BABIN¹

¹Takuvik Joint International Laboratory, Laval University (Canada)—CNRS (France), Département de Biologie et Québec-Océan, Université Laval, Québec City, Québec G1V 0A6, Canada

²DFO-MPO, Fisheries and Oceans Canada, 1 Challenger Drive, Dartmouth, Nova Scotia B2Y 4A2, Canada

³Université du Québec à Rimouski, Département de Biologie, Chimie et Géographie and BORÉAS, 300 allée des Ursulines, Rimouski, Québec G5L 3A1, Canada

⁴Sorbonne Universités, Université Pierre et Marie Curie, Paris 06, UMR 7093, Laboratoire d'Océanographie de Villefranche, Observatoire Océanologique, Villefranche-sur-Mer 06230, France

⁵Remote Sensing and Satellite Research Group, Department of Physics and Astronomy, Curtin University, Perth, WA 6845, Australia

*Corresponding author: srikanth.ayyalasomayajula@gmail.com

Received 19 January 2018; revised 12 March 2018; accepted 12 March 2018; posted 14 March 2018 (Doc. ID 320247); published 16 April 2018

In this study, we report on the performance of satellite-based photosynthetically available radiation (PAR) algorithms used in published oceanic primary production models. The performance of these algorithms was evaluated using buoy observations under clear and cloudy skies, and for the particular case of low sun angles typically encountered at high latitudes or at moderate latitudes in winter. The PAR models consisted of (i) the standard one from the NASA-Ocean Biology Processing Group (OBPG), (ii) the Gregg and Carder (GC) semi-analytical clear-sky model, and (iii) look-up-tables based on the Santa Barbara DISORT atmospheric radiative transfer (SBDART) model. Various combinations of atmospheric inputs, empirical cloud corrections, and semi-analytical irradiance models yielded a total of 13 (11 + 2 developed in this study) different PAR products, which were compared with *in situ* measurements collected at high frequency (15 min) at a buoy site in the Mediterranean Sea (the “BOUée pour l’acquisition d’une Série Optique à Long termE,” or, “BOUSSOLE” site). An objective ranking method applied to the algorithm results indicated that seven PAR products out of 13 were well in agreement with the *in situ* measurements. Specifically, the OBPG method showed the best overall performance with a root mean square difference (RMSD) (bias) of 19.7% (6.6%) and 10% (6.3%) followed by the look-up-table method with a RMSD (bias) of 25.5% (6.8%) and 9.6% (2.6%) at daily and monthly scales, respectively. Among the four methods based on clear-sky PAR empirically corrected for cloud cover, the Dobson and Smith method consistently underestimated daily PAR while the Budyko formulation overestimated daily PAR. Empirically cloud-corrected methods using cloud fraction (CF) performed better under quasi-clear skies ($CF < 0.3$) with an RMSD (bias) of 9.7%–14.8% (3.6%–11.3%) than under partially clear to cloudy skies ($0.3 < CF < 0.7$) with 16.1%–21.2% (-2.2%–8.8%). Under complete overcast conditions ($CF > 0.7$), however, all methods showed larger RMSD differences (biases) ranging between 32% and 80.6% (-54.5% – 8.7%). Finally, three methods tested for low sun elevations revealed systematic overestimation, and one method showed a systematic underestimation of daily PAR, with relative RMSDs as large as 50% under all sky conditions. Under partially clear to overcast conditions all the methods underestimated PAR. Model uncertainties predominantly depend on which cloud products were used. © 2018 Optical Society of America

OCIS codes: (010.0010) Atmospheric and oceanic optics; (010.4450) Oceanic optics; (280.0280) Remote sensing and sensors.

<https://doi.org/10.1364/AO.57.003088>

1. INTRODUCTION

Marine primary production is a key process to understanding the carbon cycle in the ocean, from the transfer of energy to high trophic levels, to the export to the deep ocean. Satellite

observations of ocean color provide a unique opportunity to derive phytoplankton primary productivity at synoptic scales. The main variables used in satellite-based primary production models are chlorophyll-a concentration, diffuse vertical light

attenuation, and incident photosynthetically available radiation (PAR).

PAR is the solar energy available for plant photosynthesis, and is defined as the radiation in the visible part of the electromagnetic spectrum (400–700 nm). PAR is expressed either in flux of photons ($\mu\text{mol photons m}^{-2} \text{s}^{-1}$), or in energy (Wm^{-2}), and constitutes 38% of the extraterrestrial incoming solar irradiance [1]. In the ocean, PAR partly controls the phytoplankton growth, upper ocean physics, and to some extent the composition and evolution of marine ecosystems [2,3]. Estimating PAR reaching the Earth's ocean surface is a key step in remote-sensing-based primary production models [4,5], and in ecosystem models [6]. PAR plays a key role in the understanding of phytoplankton dynamics, the magnitude of oceanic primary production, and the biogeochemical pump [7]. Several satellite-based primary production models use PAR at daily [8–12] and monthly [13,14] scales obtained from *in situ*, satellite measurements or radiative transfer simulations. Consequently, much of our understanding of oceanic production hinges on the quantification of solar irradiance reaching the sea surface. Therefore, it is important to accurately determine the magnitude and temporal distribution of PAR at the sea surface [15–18].

PAR can be measured *in situ* or estimated from a model fed with auxiliary data [19,20]. PAR measurements over the world oceans are scarce, so methods were developed to estimate PAR from satellite remote sensing observations [21,22]. Remote-sensing-based methods use information on the atmosphere, such as cloud optical thickness, aerosols optical thickness, and cloud fraction (CF), which are subsequently used to force a radiative transfer model (or to search in a look-up table derived from radiative transfer simulations) to obtain PAR values at Earth's surface. Look-up-table (LUT) methods based on radiative transfer models (RTMs) are computationally efficient. One advantage of the satellite-based method is that spatially continuous PAR estimates can be obtained, whereas it has the limitation to provide only instantaneous PAR values collected at the time of the satellite overpass. Some assumptions are

required to derive the daily mean values from the instantaneous values, which introduce uncertainties [21,23]. Another limitation lies in the spatial and temporal resolution of some ancillary satellite products used to estimate PAR (e.g., International Satellite Cloud Climatology Project, ISCCP, and Moderate Resolution Imaging Spectroradiometer, MODIS products) [24]. Some estimation methods are based on the extinction of PAR due to atmospheric conditions [25]. Most of these methods only describe clear-sky conditions, but a few schemes do account for the effects of clouds on PAR [26].

There are many factors affecting the attenuation of PAR through the atmosphere, including aerosol loads and their optical properties (i.e., optical depth; Ångström exponent), clouds, gaseous absorption, and sun elevation. Several radiative transfer and semi-analytical models exist to compute accurately irradiance under clear skies for given atmospheric conditions [27,28]. Of all the variables, however, sun zenith angle (θ_0) has the most extreme effect on surface irradiance along with cloud cover. In a clear sky, θ_0 affects not only the magnitude of PAR, but also the ratio between direct and diffuse components of the downward irradiance, which in turn impacts the transfer of PAR through the air-sea interface. Under cloudy conditions with optically thick clouds, θ_0 has no impact on the angular distribution of the light field due to i) the strong attenuation of the light fields by clouds, and ii) the increased scattering causing the light field to become nearly isotropic [29–31]. If we are to accurately model marine primary production at large temporal and spatial scales, the impact of clouds on the PAR reaching the sea surface should be accounted for properly. Several atmospheric [32–34] and coupled atmosphere-ocean [35] RTMs have been developed to account for the effect of clouds on surface irradiance, which in turn have been used in primary production models [13,36–39]. Several regional- and global-scale PAR products have been generated based on the methods discussed above, but most of these products have not been validated using surface observations [24]. Therefore, a systematic evaluation and comparison of these products using

Table 1. Description of PAR Estimation Methods from Different Sources and Inputs Under All Sky Conditions^a

#	PAR Model	Cloud-Correction Scheme	Input Data	Method Name	Parameters Used		
					O ₃	τ_{cl}	CF
1	OBPG Frouin <i>et al.</i>	N/A	MODIS-A L_{toa}	OBPG	✓		
2	SB	None, as in Bélanger <i>et al.</i> [18];	MODIS-A	SB_M	✓	✓	✓
3	Ricchiazzi <i>et al.</i>	Laliberté <i>et al.</i> [24]	ISCCP	SB_IS	✓	✓	✓
4		DS, for Dobson and Smith [40]	MODIS-A	SB_DS_M	✓	✓	✓
5			ISCCP	SB_DS_IS	✓	✓	✓
6		B, for Budyko [41]	MODIS-A	SB_B_M	✓	✓	✓
7			ISCCP	SB_B_IS	✓	✓	✓
8		NC (new method)	MODIS-A	SB_NC_M	✓	✓	✓
9			ISCCP	SB_NC_IS	✓	✓	✓
10	GC	DS, for Dobson and Smith [40]	MODIS-A	GC_DS_M	✓		✓
11	Gregg and Carder		ISCCP	GC_DS_IS	✓		✓
12		B, for Budyko [41]	MODIS-A	GC_B_M	✓		✓
13			ISCCP	GC_B_IS	✓		✓

^aThe acronyms correspond to the following: OBGP, Ocean Biology Processing Group; SB, SBDART radiative transfer model; GC, Greg and Carder model; IS, ISCCP dataset; M, MODIS-Aqua dataset; DS, Dobson and Smith cloud attenuation formulation; B, Budyko cloud attenuation formulation as modified by Morel and Andre [39]; NC, new cloud attenuation formulation (this study).

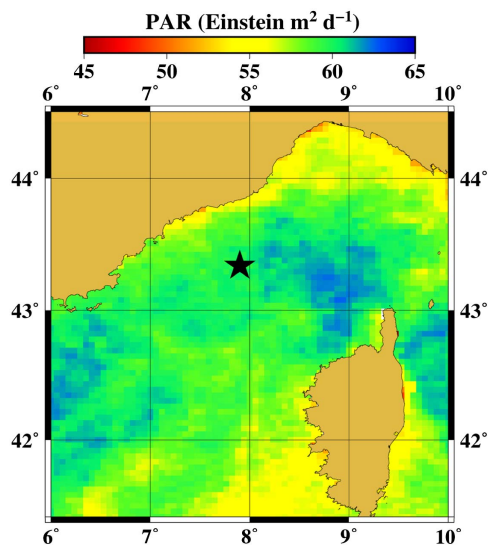


Fig. 1. Location of the BOUSSOLE site (black star). Background data corresponds to daily PAR for the month of June 2008, source MODIS L3 (Frouin and Chertok [23] algorithm).

time series of surface measurements are greatly needed, especially for peculiar cases, such as cloudy conditions and high θ_0 .

In this study, we assess the performance of 13 methods (Table 1) that retrieve PAR and are implemented in various primary production models [42], with a focus on cloudy skies and low sun elevations. The assessment was made against a large data set of multispectral irradiance data from a mooring located 55 km off the coast of France in the Mediterranean Sea ($7^{\circ}45'E$, $43^{\circ}22'N$) as part of the BOUSSOLE project [43] (Fig. 1), which includes a broad range of solar zenith angles and cloud covers.

2. MATERIAL AND METHODS

The 13 methods for estimating PAR using different combinations of models, cloud-correction schemes, and satellite products are given in Table 1. We describe them in detail in the following sections.

A. Three Radiative Models

1. NASA-OBPG

The NASA-OBPG method [44] is based on an energy budget approach, and estimates daily PAR from ocean color satellite observations. In brief, the energy reaching the surface is the initial flux that was neither reflected nor absorbed by the atmosphere-surface system. The PAR model uses plane-parallel theory, and assumes that the cloud and atmospheric components can be decoupled with no absorption by clouds in the visible region of the solar spectrum [23]. PAR is computed as the product of a clear-sky component of the atmosphere above the cloud layer and a cloud transmittance given by $1-A$, where A is the planetary albedo in the visible (i.e., surface + cloud albedo). The planetary albedo is derived from the measured TOA radiances in the visible bands. Note that the original method gives a direct estimate of $\text{PAR}(0^-)$ [23], but the OBPG PAR product is $\text{PAR}(0^+)$ following

$$\text{PAR}_{\text{cloud}}(0^+) = \frac{\text{PAR}_{\text{cloud}}(0^-)}{1 - A_S} = \text{PAR}_{\text{clear}}(0^+) \\ * (1 - A)(1 - A_S)^{-1}(1 - S_a A)^{-1}, \quad (1)$$

where $\text{PAR}_{\text{clear}}(0^+)$ is the PAR reaching the surface in the absence of clouds, $\text{PAR}_{\text{cloud}}(0^+)$ is the PAR reaching the surface under clouds, $\text{PAR}_{\text{cloud}}(0^-)$ is the PAR just below the sea surface under clouds, A_S is the ocean surface albedo, and S_a is the spherical albedo, which is stored in pre-computed LUTs [45].

2. Gregg and Carder [30]

Gregg and Carder (GC) is a clear-sky maritime spectral-irradiance model [30]. The model has fine spectral resolution of 1 nm in the 350–700 nm range.

Global downwelling solar irradiance ($E_{d\text{total}}(\lambda, 0^+)$) above the sea surface consists of the sum of two components, the spectral direct ($E_{d\text{dir}}(\lambda, 0^+)$) and diffuse downwelling irradiances ($E_{d\text{dif}}(\lambda, 0^+)$), which is expressed by

$$E_{d\text{total}}(\lambda, 0^+) = E_{d\text{dir}}(\lambda, 0^+) + E_{d\text{dif}}(\lambda, 0^+), \quad (2)$$

where λ is the wavelength (nm), and 0^+ represents the level just above the sea surface. The direct downwelling irradiance ($\text{Wm}^{-2} \text{ nm}^{-1}$) reaching the sea surface is determined through the primary attenuation processes by the spectral transmittance components in a cloud-free maritime atmosphere for Rayleigh scattering, aerosol scattering and absorption, as well as ozone, oxygen, and water vapor absorptions, using the mean extraterrestrial irradiance corrected for earth-sun distance and orbital eccentricity. The diffuse downwelling irradiance is calculated from the two spectral diffuse components induced by Rayleigh scattering, and aerosol scattering, and is given in detail by Gregg and Carder [30]. The spectral resolution is 5 nm from 400 to 700 nm, and input parameters are as given in Table 2. The total spectral irradiance, $E_{d\text{total}}(\lambda, 0^+)$, is integrated from 400 to 700 nm to yield $\text{PAR}(0^+)$. The sun angle, θ_0 , is estimated using the day of year, time, latitude, and longitude of the study site.

3. Santa Barbara Discrete Ordinate Radiative Transfer (DISORT) Atmospheric Radiative Transfer (SB) [34]

Santa Barbara DISORT Atmospheric Radiative Transfer (SBDART) is an atmospheric radiative transfer model developed by Ricchiazzi *et al.* [34]. It relies on low-resolution band models (20 cm^{-1} resolution) developed for the LOWTRAN 7 model [46]; this transmission model is represented by three-term exponential fits [47]. The equation of transfer is integrated using the well-known discrete ordinate method embodied in DISORT [48]. The discrete ordinate method provides a numerically stable algorithm to solve the equations of plane-parallel radiative transfer in a vertically inhomogeneous atmosphere. The intensity of both scattered and thermally emitted radiation can be computed at different heights and directions. SBDART is configured to allow up to 65 atmospheric layers and 40 radiation streams (40 zenith angles and 40 azimuthal modes). SBDART contains an internal database of cloud parameters (scattering efficiency, the single scattering albedo, and the asymmetry factor) for clouds composed of spherical water or ice droplets. The model contains pre-computed scattering parameters for particle size distributions with an effective radius in the range of 2–128 μm . Also,

Table 2. Meteorological and Sun Variables Represented in the Gregg and Carder Model

Parameter	Value
Pressure (P), Pa	101325
Air-mass type (AM)	1 (maritime aerosol)
Relative humidity (RH), %	80
Precipitable water (PW), cm	1
Mean wind speed (WM), ms^{-1}	4
Instantaneous wind speed (WS) ms^{-1}	6
Visibility (V), km	23
Total ozone (O_3), DU	300
Sun zenith angle (θ_o)	20°–89°

it allows for the analysis of radiative transfer through cirrus clouds, with the scattering parameters for spherical ice grains of a single-size distribution. Up to five layers of clouds are allowed, each specified by four parameters: altitude in integral kilometers, effective droplet radius, optical depth, and phase (if ice, then the effective radius is set to 106 μm). The model computes irradiance at the sea surface using the discrete ordinate method to solve the radiative transfer equation assuming a plane-parallel atmosphere for clear- and cloudy-sky conditions.

In this study, following Bélanger *et al.* [18], and Laliberté *et al.* [24], SBDART was used to generate look-up-tables of the direct and diffuse components of the incident spectral downward irradiance at the sea surface, $E_{d\text{dir}}(\lambda, 0^+)$ and $E_{d\text{dif}}(\lambda, 0^+)$, in the visible at 61 different wavelengths (i.e., every 5 nm from 400 to 700 nm), hereafter named E_d LUT, with a total of $61 \times 19 \times 10 \times 8 = 92720$ elements corresponding to 19 values of θ_o from 0° to 90° at every 5°, 10 values of total ozone concentration (O_3) from 100 to 550 in Dobson Units (DU) at 50 DU intervals, and 8 values of cloud optical thickness (τ_{cl}). Default fixed cloud properties were selected for (i) the altitude of the cloud layer (5 km), (ii) the cloud droplet effective radius (8 μm , for water clouds), and (iii) the phase function model of Henyey–Greenstein (a function of asymmetry factor; $g = 0.8$) as inputs to SBDART for the generation of LUT (Table 3).

Table 3. Input Parameters Used in SBDART Model to Generate LUT

Parameter	Values
Sun zenith angle (θ_o)	0° to 90° at every 5°
Ozone column (O_3)	100–550, at every 50 Dobson units (DU)
Cloud optical thickness (τ_{cl})	0, 1, 2, 4, 8, 16, 32 and 64
Marine aerosol	optical thickness equal to 0.1 at 550 nm defining standard vertical profiles
Mid-latitude summer atmosphere	of pressure, temperature and water vapor (McClatchey <i>et al.</i>) [49]
Altitude of the cloud layer (km)	5
Effective radius of cloud droplet (water) μm	8
Phase function model	Henyey–Greenstein parameterization [34]

The irradiances $E_{d\text{dir}}(\lambda, 0^+)$ and $E_{d\text{dif}}(\lambda, 0^+)$ are summed up and then spectrally integrated from 400 to 700 nm to obtain PAR(0^+). The sun angle, θ_o was estimated using the day of year, time, latitude, and longitude of the study site.

B. Cloud-Correction Schemes

1. Dobson and Smith Cloud Formulation [40]

The approach of DS [40], which was tuned to produce the observed monthly climatology of the mean surface irradiance, is given by

$$\text{PAR}_{\text{cloud}}(0^+) = \text{PAR}_{\text{clear}}(0^+) \times [1 - 0.53 \times (\text{CF})^{0.5}], \quad (3)$$

where $\text{PAR}_{\text{clear}}$ is the clear-sky PAR and CF is the daily mean cloud fraction. This cloud scheme is referred to as DS in model combinations.

2. Budyko (B) [41]

Morel and André [39] modified the approach of Budyko [41] for shortwave solar radiation to compute PAR(0^+) under clouds by assuming that the reduction within the spectral domain 400–700 nm due to clouds is only 75% of that of the entire solar spectrum (Eq. 4 of [39]). The PAR(0^+) is computed as

$$\text{PAR}_{\text{cloud}}(0^+) = \text{PAR}_{\text{clear}}(0^+) \times [1 - 0.29 \times (\text{CF} + \text{CF}^2)]. \quad (4)$$

This cloud scheme is referred to as B in model combinations.

3. New Cloud-Correction Schemes

Two new cloud-correction formulations were developed in the present study using daily PAR collected at the BOUSSOLE site ($\text{PAR}_{\text{in situ}}$), modeled daily clear-sky PAR ($\text{PAR}_{\text{clear}}$), and satellite-derived CF values from either MODIS-Aqua (referred to as SB_NC_M) or ISCCP (referred to as SB_NC_IS) (see Table 1). We adopted SB to calculate $\text{PAR}_{\text{clear}}$ values, since no significant differences were observed using either SB or GC in deriving the relationships. The coefficients for the new parameterization scheme were obtained from the best fit of $\text{PAR}_{\text{in situ}}/\text{PAR}_{\text{clear}}$ against CF values from MODIS and ISCCP [Figs. 7(b) and 7(c)] according to

$$\text{PAR}_{\text{cloud}}(0^+) = \text{PAR}_{\text{clear}}(0^+) \times [1 - 0.16 \times (\text{MCF}) \exp(\text{MCF})], \quad (5)$$

$$\text{PAR}_{\text{cloud}}(0^+) = \text{PAR}_{\text{clear}}(0^+) \times [1 - 0.2 \times (\text{ICF}) \exp(\text{ICF})], \quad (6)$$

where MCF and ICF are CF values from MODIS and ISCCP, respectively. The exponential function exhibited the best fit due to the non-linear distribution of CF values with $\text{PAR}_{\text{in situ}}/\text{PAR}_{\text{clear}}$ ratio.

C. Atmospheric Parameters from Remote Sensing

The ozone content, cloud fraction, and cloud optical thickness at the location of the BOUSSOLE mooring were derived from ISCCP Surface Radiative Flux and MODIS atmospheric data, which are described below.

1. ISCCP Dataset (IS)

Atmospheric parameters required to estimate the incident irradiance were obtained from the ISCCP for the BOUSSOLE location. ISCCP provides global distribution of clouds and their diurnal (3 h time resolution), as well as seasonal and interannual

variations from the analysis of satellite radiances. CF is estimated by counting the number of satellite pixels about 5 km across that are determined to be cloudy, and dividing by total number of pixels in a 280 km region (<https://isccp.giss.nasa.gov/cloudtypes.html>). Cloud properties (i.e., cloud optical thickness and cloud fraction) were retrieved from the surface radiative flux (SRF) data downloaded from the ISCCP website (<http://isccp.giss.nasa.gov/products/products.html>) [28]. The SRF dataset also includes satellite-derived, column-integrated ozone observations from the total ozone mapping spectrometer (TOMS). Global maps of ISCCP products are distributed on a 280 km resolution equal area grid at every 3 h from 1983 to 2009. The 2003 to 2009 archive was used in the present study.

2. MODIS Atmospheric Dataset (M)

The daily, 1-degree resolution (~77 km, along parallel, but ~111 km along meridian), Level-3 MODIS O₃, CF, and τ_{cl} properties were obtained from the global gridded MODIS-Aqua atmosphere products (MYD08 D3). The daily L3 CF product is derived from L2 MODIS granules acquired over a 24 h interval within the 1°-resolution pixel. In brief, each granule provides a value of 1 (cloudy) or 0 (not cloudy), and the CF is computed as the sum of all cloudy pixels divided by the sum of cloudy and clear pixels (see, MODIS ATBD for details: http://modis-atmos.gsfc.nasa.gov/_docs/L3_ATBD_C6.pdf). The data were used as inputs to retrieve PAR from the LUT method. In addition to the MYD08 D3 products used as inputs to derive PAR at the BOUSSOLE site, we downloaded the MODIS L2 PAR and CF products at 1-km resolution from an entire year (2008), $n = 363$ to assess the impact of satellite-derived CF spatial resolution on the retrieval of PAR at the BOUSSOLE site (<http://www.globcolour.info/products-description.html>). For the spatial analysis, we assumed that cloud conditions in any year would be representative of all years of MODIS observations. The CF and PAR variables were derived at 4, 8, 16, 32, 64, 80 (~1° resolution), 140, and 280 km (ISCCP, 280 km), from the 1-km resolution for 3 types of cloud cover, namely, CF < 30% ($n = 151$), 30 < CF < 70% ($n = 30$), and 70% < CF ($n = 182$). The impact of spatial scales was quantified as the absolute relative difference $\delta_{\text{PAR}} = \frac{1}{N} \sum_{i=1}^N \frac{|\text{PAR}_{(1\text{ km})i} - \text{PAR}_{(X)i}|}{\text{PAR}_{(1\text{ km})i}} \times 100$, where X correspond s to 4-km, 8-km, 16-km, 32-km, 64-km, 80-km, 140-km, and 280-km resolution.

D. Definition of PAR Products

The above detailed models, cloud-correction schemes, and the remote-sensing datasets were combined to produce 13 PAR(0⁺) products as described below.

1. OBPG Operational PAR Product

Daily Level 3 PAR data products from the Moderate Imaging Spectroradiometer (MODIS-Aqua) were downloaded from the NASA Ocean Biology Processing Group (OBPG) (<http://oceancolor.gsfc.nasa.gov>). Daily PAR values are derived using the algorithm of Frouin *et al.* [44]. The product is gridded at 4.64 km.

Daily PAR values (i.e., 24-h integration) were extracted for the BOUSSOLE's pixel (43.22° N, 7.54° E) from 2003 to 2009, and were used for comparison with *in situ* data. The

MODIS-Aqua PAR time series is a widely used dataset, which has shown good agreement when compared with *in situ* data [27].

2. LUT Method

The SBDART-based LUT method [18] described above was used to compute incident spectral downwelling irradiance at the sea surface, $E_d(0^+, \lambda, t)$, using pre-computed LUT with θ_o, O₃, and τ_{cl} as inputs and obtained from either ISCCP or MODIS-Aqua. They are referred to hereafter as SB_M, and, SB_IS methods, respectively. The PAR estimate using this method is described below.

The CF was needed to calculate the irradiance for a given ocean pixel. The CF along with O₃ was derived from ISCCP-SRF and MODIS-Atmosphere products for the BOUSSOLE pixel. Values of $E_d(0^+, \lambda, t)$, were computed for the BOUSSOLE pixel every 3 h with the ISCCP-SRF dataset, but a single daily value was obtained from the MODIS-Atmosphere dataset. Clear-sky values were obtained when CF was equal to 0. When CF was greater than 0, we applied the following equation:

$$E_d^{\text{pixel}}(\lambda, 0^+) = E_d^{\text{cloud}}(\lambda, 0^+) \times \text{CF} + E_d^{\text{clear}}(\lambda, 0^+) \times (1 - \text{CF}), \quad (7)$$

where $E_d^{\text{cloud}}(\lambda, 0^+)$ and $E_d^{\text{clear}}(\lambda, 0^+)$ were obtained from E_d LUT using the actual value of CF (for the given τ_{cl}), and CF = 0, respectively. Values of total irradiances were spectrally integrated from 400 to 700 nm to get PAR(0⁺). Thus, two SBDART PAR products, namely, SB_M, and SB_IS, were estimated for our time series.

3. Clear-Sky Models with CF Corrections

Clear-sky PAR(0⁺) obtained from the two clear-sky models (GC and SB) can be corrected for CF using the formulations of DS and B. A combination of the two models (GC and SB) and two cloud corrections (DS and B), yield four products (GC_DS, GC_B, SB_DS and SB_B). Since two sources of CF were used (ISCCP and MODIS), a total of eight models were tested (see Table 1).

DS and B were used to estimate PAR_{cloud} products using the daily mean CF inputs from ISCCP-SRF and MODIS-Atmosphere data. The daily mean CF value from ISCCP is the average of the 8 CF values (3 h resolution) available for a given day.

Table 1 summarizes the 10 combinations of clear-sky models, CF correction approaches, and atmospheric inputs that yielded 13 PAR(0⁺) products: OBPG, SB_M, SB_IS, GC_DS_M, GC_DS_IS, GC_B_M, GC_B_IS, SB_DS_M, SB_DS_IS, SB_B_M and SB_B_IS, and SB_NC_M and SB_NC_IS.

E. In Situ PAR Data for Validation

Surface downward solar irradiance data were obtained from the BOUSSOLE project [43]. The BOUSSOLE buoy provides a long-term archive, starting in 2003, of *in situ* radiometric and bio-optical quantities in support of satellite ocean-color calibration and validation activities.

The above-water downward spectral irradiance (E_s) was measured during 1 min acquisition sequences every 15 min from dawn to dusk, with a set of Satlantic OCI-200 radiometers

equipped with seven 10-nm-wide spectral bands (412 or 555, 443, 490, 510, 560, 665 or 670, and 683 nm). Instruments were factory calibrated (NIST traceable) and swapped about every six months. The E_s data processing and quality control were described in Antoine *et al.* [43]. Measurements from September 2003 to October 2009 were used in this study, which corresponds to the overlap between the MODIS and ISCCP archives.

Irradiances in $\mu\text{W cm}^{-2} \text{nm}^{-1}$ were converted into $\mu\text{mol photons m}^{-2} \text{s}^{-1}$ for all wavelengths, linearly interpolated between successive bands from 412 (or 443) to 683 nm, or linearly extrapolated towards 400 and 700 nm, and finally integrated over the PAR spectral range.

An independent Satlantic PAR sensor (400–700 nm) was also deployed on the buoy starting in September 2007. It was used to validate the PAR calculated from E_s measurements, and especially to estimate the uncertainties associated with the integration of E_d at seven wavelengths to derive PAR. The median absolute percentage deviation from the *in situ* value was found to be of 3.4% (maximum of about 7% from radiative transfer simulations) over 37,778 pairs of observations under varying solar zenith angles and sky conditions recorded between September 2007 and December 2012.

Following the spectral integration over the PAR spectrum, temporal integration was performed at a 15-min time step to retrieve daily PAR in $\text{mol photons m}^{-2} \text{d}^{-1}$. For the selected period of September 2003 to October 2009, only quality-controlled irradiance spectra with all seven wavelengths available over the entire course of the day were selected for the comparison. This step resulted in a total of 773 high-quality, daily, *in situ* data points. After a matchup exercise with MODIS-A, the data were further reduced to a final set of 729 daily *in situ* measurements. For data consistency purposes, days where either *in situ* or satellite data were missing were discarded when determining the monthly mean values. This resulted in 33 monthly average points. Further, we used a subset of 686 instantaneous irradiance measurements (in $\mu\text{mol photons m}^{-2} \text{s}^{-1}$) collected at 06 h and 18 h local time, which correspond to $\theta_0 > 70^\circ$ to investigate the performance of these models in low-angle illumination conditions. Given that the sensor used a cosine collector, the uncertainties associated with high-solar zenith angles increase from about 3% ($0 < \theta_0 < 60^\circ$) to up to 10% ($\theta_0 > 60^\circ$) as per manufacturer specifications. In addition, collectors of the sensors which, after 6-months of deployment, showed a large drift of the calibration coefficients (or, which were suspect of degradation based on a visual inspection) were systematically replaced before the final calibration.

The performance assessment for the 13 methods was carried out at daily and monthly scales, which are the most common temporal binning used by current satellite-based primary production models. Except for OBPG [44] and SB_IS [24] methods, the PAR algorithms used in satellite-based primary productivity models [42,50] have not been validated against *in situ* observations. Two semi-empirical formulations to estimate PAR corrected for cloud cover have already been compared with each other, however the performances of these methods were not assessed against *in situ* data [51].

3. STATISTICAL ANALYSIS AND METHODS RANKING

Common univariate statistical tests [52–54] were applied to test the performance of the methods.

The Pearson's correlation coefficient r is calculated according to

$$r = \frac{\sum (X^M - \bar{X}^M) \cdot (X^E - \bar{X}^E)}{\sqrt{\sum (X^M - \bar{X}^M)^2 \cdot (X^E - \bar{X}^E)^2}}, \quad (8)$$

where X is the variable. The superscript E denotes the estimated value of X (from the model), and the superscript M denotes the measured value (from BOUSSOLE buoy). \bar{X} denotes the mean value of the variable. The Pearson correlation coefficient is a measure of the strength of the linear relationship between two independent variables.

The Root Mean Square Difference (RMSD) (Ψ), which describes the uncertainty in the estimated values relative to the measured ones, was estimated according to

$$\Psi = \left[\frac{1}{N} \sum_{i=1}^N (X_i^E - X_i^M)^2 \right]^{1/2}. \quad (9)$$

The center-pattern (or unbiased) RMSD (Δ) was calculated according to

$$\Delta = \left(\frac{1}{N} \sum_{i=1}^N \{[X_i^E - \bar{X}_i^E] - [X_i^M - \bar{X}_i^M]\}^2 \right)^{1/2}. \quad (10)$$

The bias between model and measurement was estimated according to

$$\Omega = \frac{1}{N} \sum_{i=1}^N (X_i^E - X_i^M). \quad (11)$$

Note that Δ , Ψ , and Ω are related through $\Delta^2 = \Psi^2 + \Omega^2$.

Finally, the slope (S) and intercept (I) of the linear regression between estimated and *in situ* PAR(0^+) values were used to indicate the goodness of comparison of model versus *in situ* data:

$$X^E = X^M \cdot S + I. \quad (12)$$

The residual data of the simple linear regression model was calculated as the difference between the measured (X^M) and estimated (X^E) values:

$$\text{Residual} = X^M - X^E. \quad (13)$$

These statistical indicators were used to rank the methods by combining them in a quantitative statistical methodology, as in Brewin *et al.* [55]. For each model, the correlation coefficient (r), root mean square difference (Ψ), bias (Ω) and centre-pattern Root Mean Square Difference (Δ), are transformed into points as indicated below.

For the Pearson correlation coefficient (r), a test was performed to determine if the r -value for a given method was statistically higher or lower than the mean r -value of all methods. The Z_{score} method was used to determine if two correlation coefficients were statistically different from one another [56]. In brief, if we had (r_1, n_1) and (r_2, n_2) , the r -values, and the number of samples for methods 1 and 2, respectively, the

coefficients z_1 and z_2 [Eqs. (14) and (15), respectively] were computed to derive the Z_{score} according to Eq. (16):

$$z_1 = 0.5 \log \left(\frac{1 + r_1}{1 - r_1} \right), \quad (14)$$

$$z_2 = 0.5 \log \left(\frac{1 + r_2}{1 - r_2} \right), \quad (15)$$

$$Z_{\text{score}} = \frac{z_1 - z_2}{\left\{ \left[\frac{1}{n_1 - 3} \right] + [1/(n_1 - 3)] \right\}^{1/2}}. \quad (16)$$

By assuming normal distribution, Z_{score} was converted into p -value. Using a two-tailed test the r -values were considered statistically different if the p -value was <0.05 . Further, the mean r -value was estimated from all the model r -values used in the study. The r -value of each model was then compared with the mean value of all the models, to determine if the r -value of a given model was statistically lower, identical, or higher than the average value for all models.

The differences and similarities between models for Ψ and Δ were determined from the 95% confidence interval. It was assumed that the models had statistically similar differences if the 95% confidence intervals overlapped. Points were attributed to each model depending on Ψ and Δ values (as well as 95% confidence intervals) compared to mean values.

For Ω , the mean value of bias for all models was determined. It should be noted that the tests on the bias was applied to the modulus of Ω .

The scoring for the slope (S) and intercept (I) were given depending on the proximity to the average values for all models.

The points for each model were given for r , Ψ , Δ , Ω , S , and I following:

- 0 point was attributed if r is statistically lower than the mean r for all models, Ψ , Δ , and Ω are statistically higher for a model than the mean Ψ , Δ , and Ω for all models (95% confidence intervals did not overlap), and S is lower and I is higher for a model than the mean S and I for all models,
- 1 point was attributed if r is statistically identical to the mean r for all modes, Ψ , Δ , and Ω are statistically identical for a model to the mean Ψ , Δ , and Ω for all models (95% confidence intervals overlap with mean values), and S and I are identical for a model with mean S and I for all models,
- 2 points were attributed if r is statistically higher than the mean r for all models and Ψ , Δ , and Ω are statistically lower for a model than the mean Ψ , Δ , and Ω for all models (95% confidence intervals did not overlap), and S is higher and I is lower for a model than the mean S and I for all models.

To rank the performance of each method, all points were summed over each statistical test. The total score of each method was normalized by the average score of all methods. A score greater than one indicates an above average method performance, a score of one indicates that the method performance was average, and a score lower than one indicates that the method was performing poorer than average [55]. Note that the bias and RMSD were also expressed in relative unit (%) (i.e., relative bias as, $\% \text{bias} = \frac{1}{N} \sum_{i=1}^N \frac{(y_i - x_i)}{x_i} \times 100\%$, and the equivalent for RMSD) when assessing the impact of spatial and temporal resolution on daily PAR computation.

4. RESULTS

A. Methods Ranking and Performance for Daily and Monthly PAR Estimation

Figure 2 shows scatter plots of modeled daily PAR versus *in situ* daily PAR for the 11 products. It is clear from the scatter plots that all the methods perform reasonably well at estimating daily PAR(0^+) when compared with *in situ* data ($r > 0.9$, Table 4). A visual comparison of the scatter plots and the results from the points classification score (bar chart in Fig. 2), reveals that the points classification appears to be working consistently, such that the methods showing larger discrepancies and bias between estimated and *in situ* data in the scatter plots (i.e., SB_DS_M, SB_DS_IS, GC_DS_M, and GC_DS_IS) had a below average score, while methods showing a closer relationship between modeled and *in situ* data had an above-average score (i.e., OBPG, SB_M, SB_IS, SB_B_M, SB_B_IS, and GC_B_M). GC_B_IS yielded a score equal to one. Methods SB_DS_M, SB_DS_IS, GC_DS_M, and GC_DS_IS showed the poorest performance.

MODIS-A products based on the NASA-OBPG algorithm showed the highest score, while SB_IS, SB_M based on the LUT approach with ISCCP and MODIS-Atmosphere inputs, and SB and GC combined with B cloud correction using ISCCP and MODIS inputs, showed similar scores. GC_B_IS showed slightly lower score than the above-mentioned models. All clear-sky models using DS exhibited below average scores (SB_DS_M, SB_DS_IS, GC_DS_M, and GC_DS_IS).

Table 4 provides the statistics for the 11 methods at daily and monthly scales and for two new cloud parameterization methods at daily scale. At daily scale, the RMSD varied from

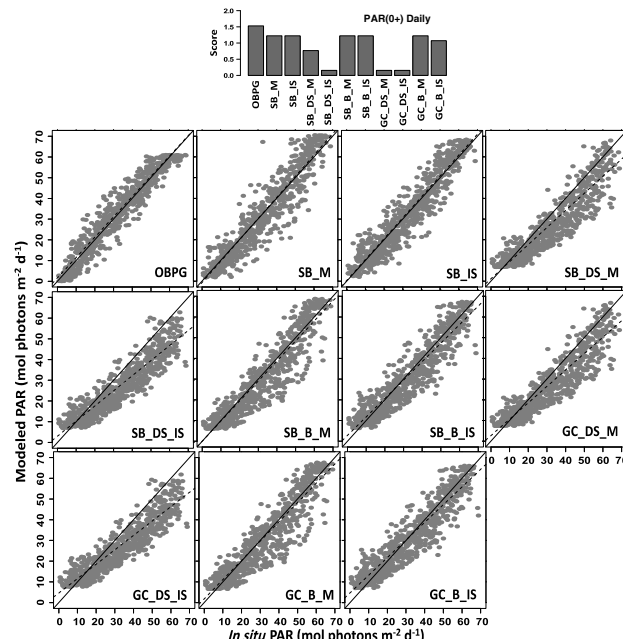


Fig. 2. Top panel: score of the 11 models used to derive daily mean PAR(0^+) (see Table 4 for model details). Bottom panels: modeled versus *in situ* PAR(0^+) for the 11 models. The solid line corresponds to 1:1 line and the dashed line corresponds to the linear fit of modeled versus *in situ* data.

Table 4. Pearson's Correlation Coefficient (r), RMSD (Ψ), CMRSD (Δ), Bias (Ω), Slope (S), and Intercept (I) Estimated Between Each Method Estimate and *In situ* for Daily and Monthly PAR Values^a

Model	Daily						Monthly					
	r	Ψ (%)	Δ	Ω (%)	S	I	r	Ψ (%)	Δ	Ω (%)	S	I
OBPG	0.96	4.91 (19.7%)	4.79	1.17 (6.6%)	0.98	1.71	0.98	3.61 (9.9%)	3.04	1.94 (6.3%)	0.98	2.49
SB_M	0.93	5.73 (25.5%)	6.73	0.16 (6.8%)	1.02	-0.67	0.98	3.28 (9.6%)	3.22	0.63 (2.6%)	1	0.29
SB_IS	0.93	5.96 (27.3%)	5.96	0.61 (11.9%)	1	0.35	0.98	3.63 (9.8%)	3.37	1.34 (3.9%)	1	0.88
SB_DS_M	0.92	8.1 (35.4%)	8.1	-4.29 (-3.7%)	0.82	1.13	0.98	5.02 (14.4%)	3.3	-3.78 (-10.3%)	0.86	0.68
SB_DS_IS	0.92	8.9 (40%)	8.9	-5.43 (-3.6%)	0.72	3.03	0.97	6.49 (16.6%)	0.19	-4.96 (-13%)	0.79	1.73
SB_B_M	0.92	6.23 (30.8%)	6.83	0.95 (10.7%)	0.96	0.05	0.98	2.89 (9%)	2.87	0.32 (0%)	0.98	0.088
SB_B_IS	0.93	6.44 (35.9%)	6.44	0.56 (19.3%)	0.89	2.82	0.97	3.21 (9.9%)	3.21	0.034 (2.7%)	0.94	1.76
GC_DS_M	0.91	8.02 (36.7%)	7.14	-3.64 (-8.7%)	0.78	2.92	0.98	6.2 (13.4%)	4.22	-4.54 (-6.9%)	0.77	2.48
GC_DS_IS	0.92	8.93 (41.3%)	7.6	-4.69 (-8.9%)	0.68	5	0.97	6.88 (16.1%)	4.95	-4.78 (-9.1%)	0.73	3.67
GC_B_M	0.92	6.36 (32.5%)	6.85	0.25 (15.9%)	0.92	1.95	0.98	3.29 (8.9%)	2.62	2 (3.7%)	0.97	2.75
GC_B_IS	0.92	6.78 (36.8%)	6.77	0.28 (24.8%)	0.84	5.11	0.97	3.75 (12.1%)	3.26	1.81 (6.7%)	0.91	4.34
SB_NC_M	0.95	5.87 (36.8%)	5.87	1.66 (27.3%)	0.97	2.4	0.98	3.87 (11.4%)	2.93	2.53 (9.9%)	1	1.31
SB_NC_IS	0.94	6.28 (43.1%)	6.28	2.25 (35.1%)	0.92	4.61	0.98	4.41 (14.5%)	3.1	3.13 (13.1%)	1	2.67

^aRMSD, CMRSD and Bias are in units of mol photons m⁻² d⁻¹. The % values refer to relative RMSD and Bias.

4.9 to 8.9 mol photons m⁻² d⁻¹, which corresponds to relative RMSD of 20 to more than 40%. The OBPG method showed the lowest relative RMSD (20%), while methods SB_M and SB_IS showed relative differences around 26%, and SB_B_M, GC_B_M showed differences around 31%. SB_B_IS, GC_B_IS, SB_DS_M and GC_DS_M showed relative RMS differences around 36%, and SB_DS_IS and GC_DS_IS showed relative RMS differences equal or greater than 40%. Methods OBPG, SB_M and SB_IS exhibited positive biases. Regarding simple cloud formulation, B-based methods (SB_B_M, SB_B_IS, GC_B_M, and GC_B_IS) exhibited positive biases, and D-based methods (SB_DS_M, SB_DS_IS, GC_DS_M, and GC_DS_IS) exhibited negative biases.

At monthly scale, relative RMSD was reduced to 8.9%–12.1% (i.e., RMSD of 2.9 to 3.6 mol photons m⁻² d⁻¹) for OBPG, SB_M, SB_IS, SB_B_M, SB_B_IS, GC_B_M, and GC_B_IS and exhibited positive biases. D-based methods (SB_DS_M, SB_DS_IS, GC_DS_M, and GC_DS_IS) showed an average of 13.4%–16.6% relative RMSD (i.e., RMSD of 5.9 to 6.9 mol photons m⁻² d⁻¹) and increased negative biases compared to daily scale.

Overall, the statistics improved when data were binned monthly (Fig. 3). In agreement with results at daily scale, results at monthly scale showed that methods based on LUT (SB_M, SB_IS), SB_B_M, GC_B_M obtained the highest scores along with OBPG, and SB_B_IS, GC_B_IS showed a score equal to one. The clear-sky model (GC) combined with B showed good performance independently of the CF input (GC_B_M, GC_B_IS). Clear negative bias was obtained when DS cloud correction was used with ISCCP and MODIS CF (SB_DS_M, SB_DS_IS, GC_DS_M, and GC_DS_IS).

B. Method Performance Under Quasi-Clear Sky, Partly Cloudy, and Overcast Conditions

From the 11 initial methods, we selected the seven best performing methods (OBPG, SB_M, SB_IS, SB_B_M, SB_B_IS, GC_B_M, GC_B_IS) based on their high scores in the objective classification (Table 4) to test their performance under different cloud conditions (we excluded methods that used the DS cloud classification, namely SB_DS_M, SB_DS_IS, GC_DS_M, and GC_DS_IS). The impact of clouds and cloud products on the performance of the seven methods was assessed for three ranges of CF: quasi-clear sky ($0.1 < \text{CF} < 0.3$), partially clear to partly cloudy ($0.3 < \text{CF} < 0.7$), and overcast ($\text{CF} > 0.7$) conditions. Results from the classification (Fig. 4) show that the performance of all of the three models and four cloud attenuation methods depends more on the cloud cover than the cloud product (i.e., MODIS versus ISCCP).

Table 5 shows the statistics of the method performance under different sky conditions. Under quasi-clear sky conditions, the relative RMSD varied from 9.7% to 14.8% (RMSD of 4.3 to 6 mol photons m⁻² d⁻¹). Based on the point classification, the OBPG method showed the best performance under

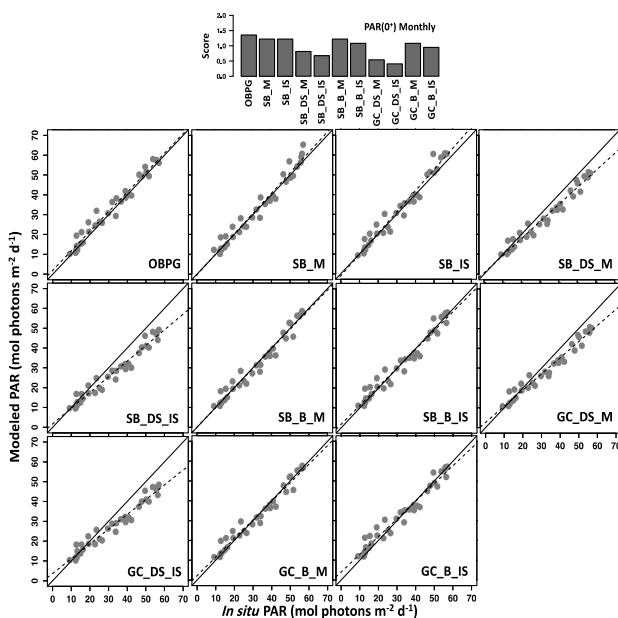


Fig. 3. Top panel: score of the 11 models used to derive monthly mean PAR(0⁺) (see Table 4 for model details). Bottom panels: modeled versus *in situ* PAR(0⁺) for the eleven models. The solid line corresponds to 1:1 line, and the dashed-line corresponds to the linear fit of modeled versus *in situ*.

Table 5. Pearson's Correlation Coefficient (r), RMSD (Ψ), CMRSD (Δ), Bias (Ω), Slope (S), and Intercept (I) Computed between Each Method Estimate and *in situ* towards the Study of Impact of Clouds and Cloud Products on PAR Values Under Different Sky Conditions^a

Model	Sky Conditions																	
	CF < 0.3							0.3 < CF < 0.7							CF > 0.7			
	r	Ψ (%)	Δ	Ω (%)	S	I	r	Ψ (%)	Δ	Ω (%)	S	I	r	Ψ (%)	Δ	Ω (%)	S	I
OBPG	0.97	4.32 (9.7%)	4.25	0.77 (3.6%)	0.95	2.64	0.94	5.72 (16.1%)	5.18	2.43 (9.2%)	0.96	3.08	0.94	5.67 (32%)	5.62	0.77 (8.7%)	1	0.47
SB_M	0.95	6.02 (13%)	5.44	2.58 (7.2%)	1	0.34	0.91	6.42 (16.3%)	6.35	-0.9 (-1.5%)	0.94	0.73	0.88	7.54 (42.7%)	7.29	-1.9 (-10.1%)	0.86	1.24
SB_IS	0.97	5.4 (14%)	4.75	2.56 (8.5%)	1	0.14	0.94	5.6 (20.1%)	5.51	1.03 (8.5%)	0.98	1.58	0.91	6.79 (47.9%)	6.55	-1.8 (-18.7%)	0.84	1.82
SB_B_M	0.97	5.17 (11.5%)	4.5	2.54 (7.8%)	1	0.42	0.94	5.18 (13.9%)	4.98	-1.5 (-2.2%)	0.88	3.03	0.9	8.73 (57.3%)	7.52	-4.4 (-20.5%)	0.6	4.45
SB_B_IS	0.96	5.06 (13.7%)	4.69	1.89 (7.4%)	1	0.69	0.94	5.59 (20.1%)	5.5	1 (4.64%)	0.86	3.55	0.9	8.23 (74.1%)	7.78	-2.7 (-45%)	0.6	6.51
GC_B_M	0.96	5.39 (12.4%)	4.38	3.13 (9.9%)	1	2.53	0.94	5.38 (14.1%)	5.27	1.08 (2.1%)	0.81	4.6	0.9	9.05 (61.6%)	8.2	-3.83 (-28.3%)	0.51	6.24
GC_B_IS	0.96	5.02 (14.8%)	4.38	2.44 (11.3%)	0.97	3.24	0.94	6.76 (21.2%)	6.75	0.47 (8.8%)	0.76	7.21	0.9	8.69 (80.6%)	8.59	-21.35 (-54.5%)	0.51	8.4

^aRMSD, CMRSD and Bias are in units of mol photons m⁻² d⁻¹. The % values refer to the relative RMSD and Bias.

quasi-clear skies (4.3 mol photons m⁻² d⁻¹ or 9.7%). The SB_M, SB_IS, and SB_B_M methods exhibited average performance, SB_B_IS showed a score equal to one, and GC_B_M and GC_B_IS exhibited below average performance.

Under partially clear to cloudy skies (0.3 < CF < 0.7) SB_M and SB_B_M methods underestimated PAR(0⁺) and all the other methods overestimated PAR(0⁺). Once again, the OBPG method exhibited the best performance, SB_IS exhibited the second-best performance, and SB_M, SB_B_M,

GC_B_M, and GC_B_IS showed below-average performance and very similar statistics. SB_B_IS showed the least performance. In general, the methods are less biased but more scattered (lower r and higher RMSD) relative to the quasi-clear sky conditions. The LUT and GC approaches (SB_B_M, SB_B_IS, GC_B_M, and GC_B_IS) combined with B showed consistent below-average scores. Under overcast conditions (CF > 0.7), the OBPG method with an RMSD of 5.67 mol photons m⁻² d⁻¹ (relative RMSD of 32%) and a positive bias

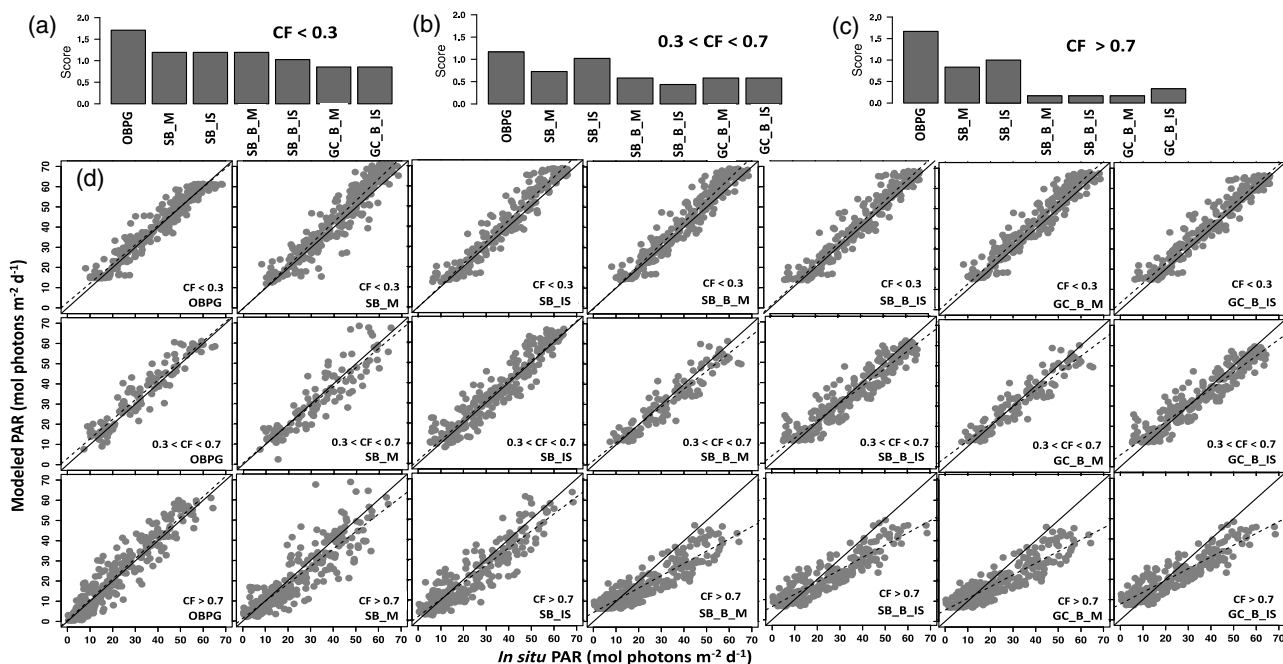


Fig. 4. Scores of the selected models used to derive daily mean PAR(0⁺) under (a) quasi-clear (CF < 0.3), (b) partially cloudy (0.3 < CF < 0.7), and (c) overcast (CF > 0.7) conditions (see Table 5 for model details). (d) Modeled versus *in situ* PAR(0⁺) for the selected models (see text for details). The solid line corresponds to the 1:1 line, and the dashed line corresponds to the linear fit of modeled versus *in situ* data.

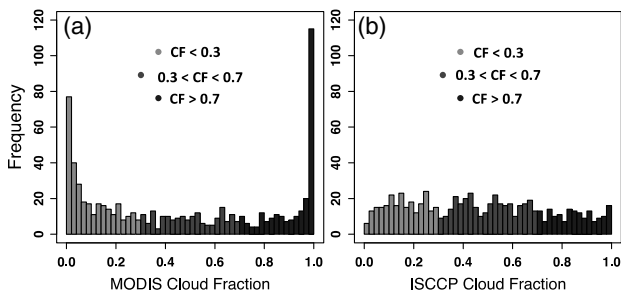


Fig. 5. Frequency distribution of (a) MODIS and (b) ISCCP daily mean CF values under quasi-clear ($CF < 0.3$), partial ($0.3 < CF < 0.7$) and overcast ($CF > 0.7$) cloud conditions.

of $0.8 \text{ mol photons m}^{-2} \text{ d}^{-1}$ (8.7%), exhibited the best performance. SB_IS exhibited the second-best performance, with RMSD of $6.79 \text{ mol photons m}^{-2} \text{ d}^{-1}$ (relative RMSD of 47.9%), followed by SB_M with RMSD of $7.54 \text{ mol photons m}^{-2} \text{ d}^{-1}$ (relative RMSD of 42.7%). For the four other models (SB_B_M, SB_B_IS, GC_B_M, and GC_B_IS), the relative RMSD varied from 57% to 80% for partly cloudy to fully overcast conditions (Table 5). The increase in model uncertainties was associated with differences in cloud products and increasing cloud cover. Under all sky conditions the NASA-OBPG method showed the best performance.

Differences in spatial and temporal resolution between MODIS and ISCCP emerged in the frequency distribution histogram of the cloud fraction (Fig. 5). First, one observes that ISCCP data showed a nearly uniform frequency distribution. In contrast, MODIS CF exhibited a bias towards clear ($CF = 0$) and overcast ($CF = 1$) sky conditions. The MODIS-Aqua CF was obtained from only one or two sensor overpasses per day at 45°N (1-km resolution average over 1° providing 1 value per day), whereas the ISCCP CF values were integrated from different meteorological sensors binned at 3 h resolution over a 280-km grid (with up to 8 values averaged over a day to get a daily CF). The differences in terms of temporal and spatial resolutions between the two satellite products had an impact on the retrieval of daily CF and consequently on PAR estimation.

C. Spatial and Temporal Mismatch

Both MODIS and ISCCP datasets contain their own limitation in terms of temporal and spatial scales, independently of uncertainties associated with the retrieval of CF, τ_{cl} . Assuming that MODIS 1-km resolution CF and PAR products represent the true values at the BOUSSOLE site, we computed the absolute relative PAR difference between the reference (i.e., MODIS 1-km resolution), and PAR, estimated at 4, 8, 16, 32, 80, 140, and 280 km resolution, to assess possible systematic bias in PAR due to spatial scales [Fig. 6(a), Table 6].

The cloud conditions were divided into three cases, namely, $CF < 0.3$, $0.3 < CF < 0.7$, and $CF > 0.7$. The mean absolute relative difference in daily PAR for $CF < 0.3$ remained lower than 10% for both MODIS (~80 km), and ISCCP (280 km) spatial resolution, with values of 6.3%, and 9.2%, respectively. For $0.3 < CF < 0.7$, the mean absolute relative difference was lower than the previous case with values of

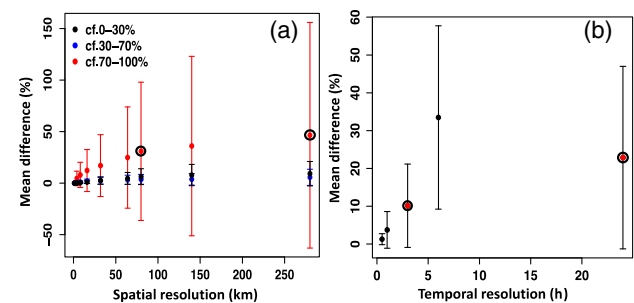


Fig. 6. (a) Mean percentage difference between daily PAR at 1-km resolution and PAR estimated at 4-km, 8-km, 16-km, 32-km, 64-km, 80-km, 140-km, and 280-km resolution for the year 2008 under varying sky conditions. The black circles correspond to MODIS (~77 km) and ISCCP (280 km) spatial resolutions. The black, blue, and red vertical bars represent the lower and upper limits of the mean error for the three sky conditions (see text for details). (b) Mean percentage difference between daily integrated PAR at 15 min time step and daily integrated PAR at 30 min, 1 h, 3 h, 6 h, and 24 h time step for two months of BOUSSOLE buoy data under all sky conditions. The black circles correspond to ISCCP (3 h binning) and MODIS (24 h binning) temporal resolutions. The black vertical bars represent the lower and upper limits of the mean error.

3.6%, and 4.7% for MODIS and ISCCP dataset, respectively. In overcast skies ($CF > 0.7$), the mean absolute relative difference increased to $31 \pm 55\%$ for MODIS spatial resolution, and to $46 \pm 100\%$ for ISCCP spatial resolution. The ISCCP 280 km resolution exhibited systematic larger difference than the MODIS 1° resolution.

The impact of temporal integration on daily PAR was assessed by computing the difference between daily integrated PAR at 15 min resolution with daily integrated PAR at, 30 min, 1 h, 3 h, and 24 h time steps for 61 days of data collected at BOUSSOLE. For the single day measurement (i.e., MODIS 24 h single pass), we scaled the clear-sky, 15 min resolution PAR to the value at 13 h30, which corresponds roughly to the time of the MODIS pass, from which we computed the daily PAR using a 15 min time step [Fig. 6(b) and Table 6].

Table 6. Comparison of Mean Differences of Daily Integrated PAR Modeled and Estimated Under Different Spatial and Temporal Binning for MODIS ($1^\circ \sim 77 \text{ km}$; 24 h) and ISCCP ($2.5^\circ \sim 280 \text{ km}$; 3 h)^a

PAR	Mean Absolute Difference (%)			
	(Mean Difference (%))	$CF < 0.3$	$0.3 < CF < 0.7$	$CF > 0.7$
Difference Due to Spatial Mismatch				
1 deg (~77 km)	6.3 ± 7	3.6 ± 5	31 ± 55	
	-6.2 ± 14	(-2.4 ± 8)	(17.2 ± 54)	
280 Km	9.2 ± 11	4.7 ± 8	46 ± 100	
	(-9.2 ± 22)	(-5 ± 7)	(31.8 ± 96)	
Difference Due to Temporal Mismatch				
24 h		20 ± 25	(3.3 ± 12)	
3 h		10 ± 11	(0.47 ± 32)	

^aThe values are given in relative units.

During these 61 days, the daily PAR varied between 1.5 and 55 mol photons $m^{-2} d^{-1}$, which attested to various sky conditions, namely, 24 days with $CF < 0.3$, 13 days with $0.3 < CF < 0.7$, and 24 days with $0.7 < CF$, based on MODIS cloud fraction values. The ISCCP 3 h integration time step induced a 10% absolute relative difference when compared to the 15 min integration time, whereas the single daily measurement of MODIS induced a mean percentage error of 20%. Similarly, the absolute relative differences (expressed in % and referred to as δ_{PAR}), which expressed biases (without modulus in the equation $\delta_{PAR} = \frac{1}{N} \sum_{i=1}^N \frac{(PAR_{(1\ km)} - PAR_{(X)_i})}{PAR_{(1\ km)_i}} \times 100$), showed that the biases were all of the same sign under $CF > 0.7$, both for spatial mismatch and under temporal mismatch, in comparison to relative absolute differences. For $CF < 0.3$ and $0.3 < CF < 0.7$, however, the sign of the biases was negative (the values of biases are given in brackets in Table 6).

D. New Cloud-Correction Parameterization

Comparison of the new cloud-correction parameterization with the B and DS methods is shown in Fig. 7(a). As expected from the results presented above (i.e., PAR underestimation under

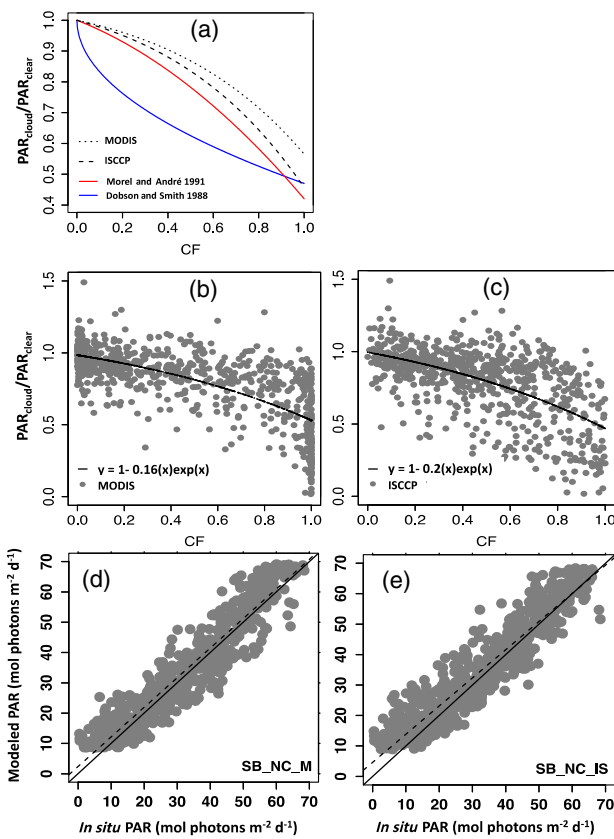


Fig. 7. (a) Ratio PAR_{cloud}/PAR_{clear} as a function of CF for B (solid red line), DS (solid blue line), and the new cloud-correction schemes (dashed line for ISCCP and dotted line for MODIS datasets). Ratio PAR_{cloud}/PAR_{clear} as a function of CF for (b) MODIS and (c) ISCCP. The black solid line corresponds to the fitted relationships proposed in this study. Modeled versus $in situ$ PAR(0^+) for the new cloud-correction schemes for (d) MODIS and (e) ISCCP products. The solid lines in (d) and (e) corresponds to 1:1 line and the dashed line correspond to the linear fit of modeled versus $in situ$ data.

cloudy conditions), the PAR attenuation by clouds was lower (i.e., PAR values are higher) for a given value of CF with the new parameterizations compared to B and DS.

The statistical performance of the methods is summarized in Table 4. Method SB_NC_M showed the best performance after OBPG with a higher r (0.95) and RMSD of 5.87 mol photons $m^{-2} d^{-1}$. Evaluation of the daily PAR values against $in situ$ PAR provides relative RMSD (bias) values of 36.8% (27.3%) for SB_NC_M [Fig. 7(d)], and, 43.1% (35.1%) for SB_NC_IS [Fig. 7(e)], respectively. At monthly scale, the relative RMSD values reduced to 11.4%, and 14.5%, for SB_NS_M, and, SB_NC_IS, respectively. The better performance of the new cloud-correction parameterizations (NC) compared to DS and B methods can be attributed to the fact that the new method was validated using the same dataset used to develop it.

E. Instantaneous PAR Estimation Under Low Sun Elevation

A total of 686 $in situ$ instantaneous irradiances were used to assess the performance of four models under low sun elevations, a situation prevailing at high latitudes. Methods SB_IS, SB_DS_IS, SB_B_IS, and SB_NC_IS were selected because they allow estimations of instantaneous PAR. ISCCP CF was used as input for this exercise because it provides updated cloud properties every 3 h from 00 h to 24 h. Instantaneous irradiances at 06 h and 18 h were used, corresponding to low sun elevations in the range 0° – 20° [corresponding to Solar Zenith Angle (SZA) range 70° – 90°] at the BOUSSOLE site.

Under all sky conditions the four methods performed reasonably well ($r > 0.85$) at estimating the instantaneous irradiances, but tended to show a large discrepancy with a mean relative RMSD value of 50% or more (Fig. 8, Table 7). The four methods show statistically similar performances. However,

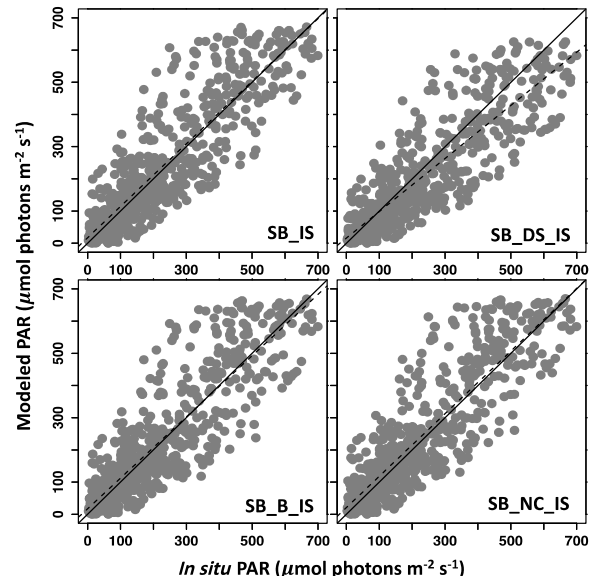


Fig. 8. Modeled versus $in situ$ instantaneous PAR(0^+) for the four methods (see Table 7 for model details). The solid line corresponds to the 1:1 line, and the dashed-line corresponds to the linear regression of modeled data versus $in situ$ data.

Table 7. Pearson's Correlation Coefficient (r), RMSD (Ψ), CMRSD (Δ), Bias (Ω), Slope (S), and Intercept (I) Computed between Each Method Estimate and *In Situ* Data Under All Sky Conditions for Low Sun Elevations^a

Model	r	Ψ (%)	Δ	Ω (%)	S	I
SB_IS	0.88	92.5 (55.1%)	91.91	11 (23.2%)	0.97	17.03
SB_DS_IS	0.86	92.4 (50.7%)	89.15	-24 (-6.4%)	0.82	16.07
SB_B_IS	0.87	94.7 (55.4%)	94.51	6 (21.5%)	0.95	17.33
SB_NC_IS	0.88	94.8 (57.2%)	93.7	14 (27%)	0.97	20.6

^aRMSD, CMRSD and Bias are in units of in $\mu\text{mol photons m}^{-2} \text{s}^{-1}$. The % values refer to the relative RMSD and Bias.

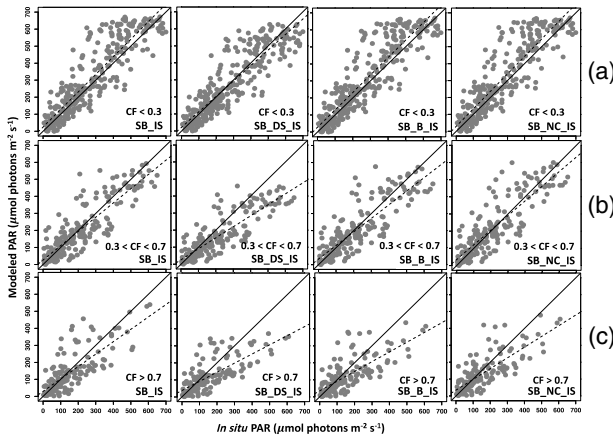


Fig. 9. Modeled versus *in situ* instantaneous PAR(0^+) for SB_IS, SB_DS_IS, SB_B_IS and SB_NC_IS under (a) quasi-clear ($CF < 0.3$), (b) partially cloudy ($0.3 < CF < 0.7$) and (c) overcast ($CF > 0.7$) conditions (see Table 8 for details). The solid line corresponds to the 1:1 line and the dashed-line corresponds to the linear fit of modeled versus *in situ* data.

methods SB_IS, SB_B_IS, and SB_NC_IS show positive biases with a slope close to 1, whereas SB_DS_IS exhibits negative bias and a slope well below 1 (i.e., 0.82), similar to the results obtained in daily and monthly comparisons.

The accuracy of the model estimates was also assessed under different cloud conditions, in order to test the applicability of

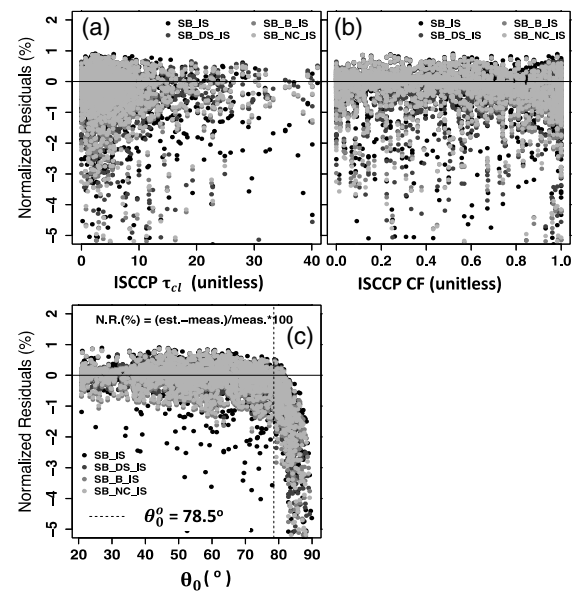


Fig. 10. Normalized residuals of the four methods (see Table 7 for model details) as a function of (a) ISCCP τ_{cl} , (b) ISCCP CF, and (c) θ_0 . Vertical dashed line in (c) corresponds to sun zenith angle of 78.5° , and the solid black line corresponds to a percentage residual equal to zero.

the methods in regions with more persistent cloud covers (results in Fig. 9 and Table 8). Under clear-sky conditions the SB_B_IS method showed better performance with lower model uncertainties ($53.2 \mu\text{mol photons m}^{-2} \text{s}^{-1}$), compared to the SB_IS ($100 \mu\text{mol photons m}^{-2} \text{s}^{-1}$), SB_DS_IS ($86.7 \mu\text{mol photons m}^{-2} \text{s}^{-1}$), and SB_NC_IS ($103 \mu\text{mol photons m}^{-2} \text{s}^{-1}$) methods. Under partially cloudy and overcast conditions, the SB_B_IS approach also performed better than the SB_IS and SB_DS_IS methods. It is noteworthy that for $CF > 0.3$, all the methods showed a negative bias.

The relationship between normalized residues [i.e., $(\text{Estimated}-\text{Measured})/\text{Measured} * 100$], and θ_0 , τ_{cl} and CF is shown in Fig. 10. For $\theta_0 > 70^\circ$, the four methods showed a tendency to underestimate PAR. It can be clearly observed from Fig. 9, that the increase in PAR underestimation was

Table 8. Pearson's Correlation Coefficient (r), RMSD (Ψ), CMRSD (Δ), Bias (Ω), Slope (S), and Intercept (I) Computed Between Each Method Estimate and *In Situ* Data Under Different Sky Conditions for Low Sun Elevations^a

Model	Sky Conditions																	
	CF < 0.3				0.3 < CF < 0.7				CF > 0.7									
Model	r	Ψ (%)	Δ	Ω (%)	S	I	r	Ψ (%)	Δ	Ω (%)	S	I	r	Ψ (%)	Δ	Ω (%)	S	I
SB_IS	0.89	100.19	94.37	33.64	1	21.5	0.86	84.46	83.86	-9.32	0.83	26.14	0.77	85.46	84.61	-11.98	0.72	29.89
		(44.5%)		(21.8%)				(64.8%)		(-9.3%)				(65.3%)		(-18.2%)		
SB_DS_IS	0.89	86.75	86.69	-3.21	0.9	22.02	0.85	100.61	86.41	-51.53	0.64	25.93	0.74	93.01	86.53	34.1	0.53	37.4
		(39%)		(-6.8%)				(59.8%)		(-40.3%)				(63.9%)		(-8.1%)		
SB_B_IS	0.99	53.23	34.57	40.48	0.88	-1.31	0.89	59.9	40.26	-44.35	0.77	7.55	0.86	34.57	40.43	-16.19	0.76	19.94
		(44.9%)		(22.4%)				(65.3%)		(-29.2%)				(64.8%)		(-9.6%)		
SB_NC_IS	0.89	103.28	95.8	38.29	1	29.5	0.86	87.98	87.9	-2.91	0.85	35.15	0.77	81.31	81.3	-21.7	0.63	34.5
		(45.2%)		(24.3%)				(68.9%)		(-8.2%)				(65.4%)		(-18%)		

^aRMSD, CMRSD and Bias are in units of in $\mu\text{mol photons m}^{-2} \text{s}^{-1}$. The % values refer to the relative RMSD and Bias.

pronounced under partially cloudy to overcast conditions. It should be noted that 2490 instantaneous irradiances were used to study the relationship between normalized residuals and θ_0 , τ_{cl} , and CF, corresponding to SZA range 20°–90°.

5. DISCUSSION

A. Performance of PAR Estimation Methods Under All Sky Conditions, Temporal and Spatial Mismatch

The consistent performance of the NASA-OBPG method in all sky conditions (i.e., from clear to cloudy skies) can be partly attributed to the high spatial resolution of the satellite pixel (4.6×4.6 km), which better represents the atmospheric conditions around the point of observation. Our sensitivity study on spatial scales showed that for all sky conditions, the mean absolute relative error (δ_{PAR}) remains below 5%. The good performance of the OBPG method is explained by the energy budget approach, which does not require knowing whether a pixel is clear or cloudy, i.e., it avoids making some arbitrary assumptions about cloudiness. The good performance of the NASA-OBPG PAR model has also been reported in a recent study [24] that used ship-based irradiance measurements collected in the Canadian Arctic.

The relatively good performance ($r > 0.9$) of the LUT methods using both ISCCP-SRF (relative RMSD ~ 27%) and MODIS (relative RMSD ~ 25%) products likely results from an accurate solution of the radiative transfer equation and explicitly accounting for the effects of atmospheric conditions (i.e., CF, τ_{cl} and O_3) over the study region.

Both OBPG and LUT methods, based on different radiative transfer models and approaches, exhibited positive biases in all sky conditions. In the case of OBPG, this positive bias may be explained by (i) the single satellite pass near local noon, i.e., when cloudiness is generally reduced, (ii) a possible overestimation of the clear-sky values, (iii) a small bias in the calculation of spectrally integrated transmittance (of cloud/surface) functions, and (iv) the correction of large scattering by molecules and aerosols in the presence of clouds considering the decoupling of clear atmosphere and the cloud-surface effects assuming that the cloud-surface layer is located below the clear atmosphere [57]. In the case of the LUT methods based on the RT model, the positive biases could be attributed to the overestimation of the radiation (especially in the diffuse part of shortwave) due to: (i) the errors in the selection of the aerosol scattering parameters, (ii) neglecting the continuum absorption process at visible wavelengths, and (iii) the use of a constant atmospheric transmission coefficient in the RT model simulations [34]. The results (Table 4) show that when PAR is integrated over a month, the performance of both OBPG and LUT methods improved in terms of RMSD, but the positive bias remained unchanged [27]. In addition, one cannot exclude the possibility that a bias in *in situ* measurements exists, which, in the present study relied essentially on the calibration provided by the manufacturer.

From Fig. 6 and Table 6 it can be observed that, in clear ($CF < 0.3$) and cloudy skies ($CF < 0.7$), the temporal resolution induced higher uncertainties for both ISCCP and MODIS CF than spatial resolution. The absolute δ_{PAR} values due to spatial mismatch remains below 6.3% and 9.2%, while the

temporal mismatch reached 20%, and 10%, for MODIS single pass, and ISCCP 3-h resolutions, respectively (Table 6). This suggests that in clear skies and partially cloudy skies, the uncertainties in PAR retrieval are driven by the temporal mismatch between the *in situ* and satellite data. In overcast conditions ($CF > 0.7$), the low spatial scales of MODIS (1°) and ISCCP (280 km) datasets become a more important source of uncertainties than the temporal mismatch with respective absolute δ_{PAR} values of 31%, and 46%, respectively (Table 6). These values are close to the relative RMSD values of both LUT MODIS (42.7%) and LUT ISCCP (47.9%) under overcast conditions (Table 5). MODIS cloud products, despite a lower temporal resolution than ISCCP cloud products, led to better PAR estimations as given by their lower RMSD values due to a better spatial resolution. Laliberté *et al.* [24] reported large discrepancies between OBPG and LUT with ISCCP models in the Arctic Ocean. The better performance of the LUT method reported here, as compared to the performance reported in Laliberté *et al.* [24] may be explained by the accuracy of the ISCCP products, since cloud properties above 60° latitude are solely derived using data from the polar-orbiting satellites [57], whereas below that latitude, geostationary satellites also contribute to the ISCCP dataset.

The model uncertainties were reduced when using the monthly time scale, and the performance of the models was significantly improved. This could be attributed to the compensation of spatial scale discrepancies (satellite versus *in situ* data) from daily to monthly values. A recent study emphasized that accounting for statistical diurnal cloud variability increased the scatter between estimated and measured PAR values on a daily time scale, but reduced the bias and improved the agreement between modeled and measured PAR on a monthly time scale [57]. Negative and positive daily biases can also compensate each other when integrated over an entire month.

The empirical formula [Eq. (4)] for cloud correction provides a simple approach to account for the impact of clouds on daily and monthly PAR estimations. It proved to be successful in primary production models when the clear-sky PAR has been accurately estimated [13]. However, published empirical parameterizations (DS and B) tend to underestimate PAR under cloudy condition (i.e., overestimate the cloud attenuation) (see below). In particular, DS formulation showed poor performance when compared to the other approaches. This is explained by the mathematical formulation of the model (square root), which results in a rapid decrease of PAR with increased CF compared to other formulations [Fig. 7(a)].

B. Impact of Clouds and Cloud Products on PAR Estimation

Clear-sky models coupled to B tended to underestimate PAR as CF increased (Fig. 4 and Table 5). This became obvious under high CF and high *in situ* irradiance (e.g., cloud cover in spring and summer). However, B tended to overestimate PAR at the lower range of *in situ* PAR values (<15 mol photons m⁻² d⁻¹). This feature may be seasonal (PAR overestimation in winter and PAR underestimation in summer), and perhaps related to cloud types, e.g., more frequent haze or thin clouds in winter, which was not taken into account by these models.

The Morel and André [39] approach was derived from Budyko's formulation [41] for the shortwave radiation and modified to compute PAR(0^+) (400–700 nm). Budyko's formulation, developed using monthly mean cloud estimates as a function of latitude and the CF, does not account for cloud type and seasonal variations in solar elevations [40]. B formulation performed better than DS, with a large underestimation of PAR by DS in the high range of values. Differences between DS and B in the fraction of PAR transmitted to the surface in presence of clouds (i.e., PAR_{cloud}/PAR_{clear}), were larger than 10% [Fig. 7(a)] when CF ranges from 0.05 to 0.7. The largest difference, about 17.7%, occurred for CF equal to 0.3. For CF > 0.8, both DS and B yielded similar PAR_{cloud}:PAR_{clear} ratios. The consistency between B and NC parameterizations emphasizes the reliability of empirical models to retrieve PAR at the sea surface. The better results obtained by NC can be explained first by the fact that the parameterization was developed using the same dataset as for validation, and second, by the use of an exponential term in the formulation to simulate the rapid decrease of the PAR_{cloud}:PAR_{clear} ratio with increasing CF. To some extent, it is not surprising to see some simple parameterization (e.g., NC) performing similarly to more advanced methods, such as LUT, generated by using the radiative transfer model, since PAR at the sea surface becomes negligible for large cloud optical thickness. For instance, for a cloud of 1-km thickness with an optical thickness of 4.6, only 1% of the light would reach the surface such that the CF becomes prevalent over the optical thickness. The average cloud optical thickness at the BOUSSOLE site is about 15 (source: <https://giovanni.gsfc.nasa.gov/giovanni> for the period January 1st, 2003 to December 31st 2016), which is well above 4.6.

We expected a better performance of empirical cloud correction using high spatial resolution CF data (i.e., 1° versus 280 km). Surprisingly, the RMSD were similar for both MODIS-Aqua and ISCCP CF products, as well as the goodness of the fit (similar r and RMSD), despite the large difference in their spatial resolution (82 versus 280 km). The sensitivity study carried out on the mismatch in spatial scales revealed that the uncertainties increased with increasing cloud fraction to reach almost 50% for CF > 0.7.

The OBPG and MODIS-based daily PAR estimates were obtained from instantaneous PAR measurement collected from a single daily pass. This implied that the cloud system remained constant during the day. As a consequence, if the sky was clear at the time of the MODIS-Aqua observation, PAR would be overestimated if clouds were present at other times of the day. Similarly, PAR would be underestimated when the sky is cloudy during the satellite pass, but mostly clear during the rest of the day. In addition to spatial resolution, some of the uncertainties are likely due to a lack of information on diurnal variability [23,27,44].

Unlike MODIS observations, the ISCCP dataset provides a good representation of the diurnal variability of clouds at relatively high temporal resolution. The low spatial resolution, however, smoothens cloud variability (i.e., broken clouds against continuous cover) such that at a given time, the buoy might be under direct sunlight but the ISCCP observations will yield a percentage of cloud cover. This explains some of the

variability observed when comparing the PAR derived using the ISCCP cloud dataset and *in situ* measurements.

C. Impact of Low Sun Elevations on PAR Estimation

Low sun elevations (>70°) prevail during dawn and dusk in any given location, during winter time at mid latitudes and most of the year in polar regions, which makes the accurate estimation of PAR challenging.

All methods based on LUT underestimated PAR when θ_0 reached more than 78.5° (Fig. 10). This underestimation at low sun elevations may have two origins. First, from a radiative transfer modeling perspective, SBDART solves the radiative transfer equation for a plan-parallel geometry and isotropic surface-reflected radiation. These assumptions fail to account for broken clouds in the atmosphere. For example, the direct component of PAR may be very sensitive to partial clouds. In addition, large deviations from Lambertian reflection may occur when very high specular reflection dominates the surface albedo [34] thus, leading to uncertainties in determining surface reflectance. This process would be more important under windy conditions. Second, cloud optical thickness and cloud fraction retrievals in the ISCCP product can be biased and have limitations when the solar zenith angle exceeds 78.5° [58]. This explains the scatter and deviations from the 1:1 line at lower elevations in the four models tested (i.e., SB_IS, SB_DS_IS, SB_B_IS and SB_NC_IS)). The ISCCP dataset assumes that the cloud distribution was homogeneous in partially cloudy pixels. Thus, horizontal cloud heterogeneities may result in over or underestimation of the PAR(0^+) depending on cloud type, sensor resolution, and observing geometry. Retrieval of cloud optical thickness with low spatial resolution leads to underestimation, which results in overestimation of PAR [59,60]. Some of the discrepancy between measured and modeled values may be attributed to the cloud type, however, the nature of our cloud datasets does not give us the opportunity to investigate this further in the current study.

D. Methods Ranking

The methods ranking criteria used in our study helps quantitative comparison between different methods. However, the criteria itself may need to be considered carefully with changing user requirements.

For instance, the baseline usage of average performance of all methods to compare PAR product performance may be altered by poorly performing methods (i.e., skewing model result distribution), making it difficult to discriminate between the higher performing methods. In the present study, DS-based cloud-correction methods showed very poor performance with high Ψ , Δ , and high negative Ω , in comparison with other methods under daily scales (see Fig. 2). This results in the minimal points to the methods SB_DS_M, SB_DS_IS, GC_DS_M, and GC_DS_IS, and maximum points for all other methods.

However, when these four methods are excluded from the analysis (Fig. 11), the OBPG remains the best performing method, SB_M, SB_IS, SB_B_M, and SB_B_IS show average performance with a score equal to 1, and other methods show below-average performance. This demonstrates that the method remained robust in our analysis. In general, one should be cautious in using the average performance of all methods as a

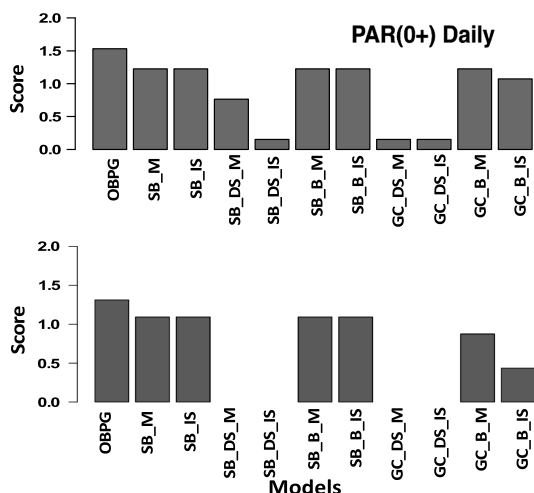


Fig. 11. Method scores with (top) and without (bottom) the inclusion of SB_DS_M, SB_DS_IS, GC_DS_M, and GC_DS_IS methods.

baseline towards comparing performance of the methods, since it only indicates the relative performance of individual method with respect to others, and not in absolute terms.

6. SUMMARY AND CONCLUSIONS

Reliable modeling and monitoring of marine primary production require high accuracy PAR estimates. Here, an objective classification was used to assess and rank methods to compute PAR at daily and monthly scales based on their quantitative performance derived from a set of univariate statistics. Eleven PAR estimation methods were ranked by comparison with *in situ* data collected at the BOUSSOLE site. Among these 11 methods (excluding two new methods), seven methods were further selected to study the impact of clouds formulation (i.e., a simple equation or radiative transfer computation), properties, and data source (i.e., MODIS versus ISCCP) on the accuracy of PAR(0^+) retrieval. In addition, the performance of four approaches that yield instantaneous PAR(0^+) was tested for low sun angles.

The first objective of evaluating PAR under daily and monthly scales revealed that the OBPG approach ranked first with uncertainty of 20%, and LUT (ISCCP and MODIS) approaches showed second-best performance with uncertainty of around 26% on daily scales, respectively, and uncertainties of 10% for the same approaches on monthly scales. Using empirical cloud-correction methods, B method exhibited uncertainties of 30%–35% and 9%–12%, and DS had 35%–40%, and 14%–16%, at daily and monthly scales, respectively. Uncertainty of these methods can be slightly reduced, and the bias removed, using a regionally tuned cloud correction. This parameterization of cloud attenuation would require further evaluation at other oceanic sites to assess its range of applicability.

Uncertainties in PAR estimates at the sea surface resulted mainly in the differences in spatial and temporal resolution of the atmospheric inputs. We showed that under clear and cloudy sky conditions ($CF < 0.7$), the temporal resolution (3 h and 24 h)

was the main source of error. In overcast conditions, the spatial scales of MODIS and ISCCP cloud products (1° and 280 km, respectively), became the main source of uncertainties. Other factors that affected the uncertainties in the retrieval of PAR were the use of the plane-parallel atmospheric radiative transfer model to generate look-up-tables, which failed to account for broken clouds in the atmosphere, and uncertainties in determining surface reflection. In fact, methods that used satellite data with coarse pixel resolution may depict bulk PAR for areas larger than a single discrete station.

The second objective of the study was to address the impact of different cloud products on PAR estimates. The individual methods showed relative RMSD that varied with cloud conditions from 9% to 14% (for $CF < 0.3$), 16% to 21% (for $0.3 < CF < 0.7$), and 32% to 80% (for $CF > 0.7$), revealing a trend of decreasing performance with increasing cloud cover. The RMSD differences also responded differently to cloud products (i.e., MODIS versus ISCCP).

Finally, the study focused on PAR estimation under low sun elevation, including cloud conditions. The relative uncertainty of 55% for the LUT method under low sun elevations was larger than the value of 33% reported by Laliberté *et al.* [24] in the Arctic Ocean. The result indicated a rapid decrease in model performance for solar zenith angles higher than 78° .

We selected only algorithms that have been used in published marine primary production models and assessed their performance in clear and cloudy skies, and at low sun elevations. We showed that the current OBPG algorithm performed well in all sky conditions, however it is limited to a single measurement per day that is extrapolated to the entire day, which adds uncertainties to the calculation of daily PAR(0^+) and notably for application to primary production computation when short term variation in PAR induces rapid non-linear changes in phytoplankton physiology and production. It should be noted that at high latitudes, daily PAR estimates from multiple passes and multiple polar orbiters may reduce uncertainties due to diurnal variability of clouds. The method based on look-up-tables also showed consistent results with *in situ* measurements and provided the advantage of capturing daily variations with the appropriate inputs. It would be the most adapted model if spatial and temporal resolution were improved, especially for the estimation of primary production. In the current study, the ISCCP model had the highest temporal resolution ("three hours"). One can anticipate that a finer temporal resolution would improve the accuracy of daily PAR(0^+). The use of clear sky model corrected for cloud using simple formulation exhibited slightly higher difference than the previous method but their ease of application is an asset that should not be overseen, as evident from various studies [61–65]. It should be noted that a model that considers parameterization of clouds alone with cloud fraction as the only variable does not take into account the essential physics in PAR(0^+) estimation. Because cloud transmittance is the other important variable under cloudy skies, and can vary depending on cloud optical thickness, such parameterization should be used with caution based on local conditions.

Although the BOUSSOLE buoy is located at mid-latitude ($\sim 45^\circ N$), one of the objectives of our study was to evaluate the

performance of those algorithms in conditions that are frequently encountered at high latitudes where cloud cover and low sun elevations are frequent [38]. We acknowledge that the types of clouds found at high latitudes do differ from those found in the BOUSSOLE area. Also, the impact of haze (which is another common feature above Arctic waters) on the PAR reaching the sea surface was not considered, given that no satellite observations of such atmospheric conditions currently exist. Nevertheless, the present study is a first step in thoroughly assessing and understanding the limitation of PAR algorithms under a variety of cloud coverage and low sun elevation.

It is likely that the results derived from the current study at a single site can be extrapolated to other regions. The quantification of the uncertainties will probably change with location (i.e., increase with increasing latitude and cloudy sites), but we are confident that the overall comparison between models would hold given that we have assessed various cloud covers and sun angles, and that the radiative transfer model would provide similar results in similar atmospheres independently of locations.

The quantified PAR uncertainties suggest that adequate representation of clouds and their properties both on spatial and temporal scales are significant. Also, more efforts to quantify uncertainties under low sun elevations by more evaluation studies in different regions and time scales are necessary in accurate estimations of PAR, which is important for primary production studies. A major effort towards considering the representation of diurnal-cycle measurements with hourly changes in irradiance fields (e.g., due to clouds) improves daily integrated PAR values.

An interesting future perspective is to combine the available Geostationary and Polar-orbit Ocean Color satellites' data that will be able to capture hourly variations in cloud cover, which may improve the model's performance. The surface albedo may cause great uncertainties under cloudy conditions, hence the parameterization of the method for different sea-surface conditions would be useful in future studies. The LUT method had the ability to decompose total irradiance into direct and diffuse components, an important aspect when deriving PAR just below the sea surface from PAR just over the sea surface to account for Fresnel reflection of direct and diffuse components. The OBPG method directly estimates PAR below surface (a factor of $1 - A_s$, is introduced to estimate PAR above surface from PAR below surface). Our study showed that under given conditions, simple cloud formulations perform similar to more complex models. The next step would be to assess possible improvements, and gain in PAR retrieval accuracy when using complex approaches that would use supplementary ancillary data, such as cloud altitude, cloud phase, and mean cloud droplet size [66].

Funding. Canada Excellence Research Chairs, Government of Canada (CERC); Fonds de Recherche du Québec—Nature et Technologies (FRQNT); Centre National de la Recherche Scientifique (CNRS); Université Laval; Canadian Network Centre of Excellence ArcticNet; Natural Sciences and Engineering Research Council of Canada (NSERC); Canadian Space Agency (CSA).

Acknowledgment. Srikanth Ayyala Somayajula received a postgraduate scholarship from CERC in Remote Sensing of Canada's New Arctic Frontier and stipends from Québec-Océan. The authors gratefully acknowledge the BOUSSOLE project team for collecting, processing, and archiving the *in situ* buoy data.

REFERENCES

1. J. T. O. Kirk, *Light and Photosynthesis in Aquatic Ecosystems*, 2nd ed. (Cambridge University, 1994).
2. P. G. Falkowski, R. T. Barber, and V. Smetacek, "Biogeochemical controls and feedbacks on ocean primary production," *Science* **281**, 200–206 (1998).
3. S. M. Vallina, M. J. Follows, S. Dutkiewicz, J. M. Montoya, P. Cermeno, and M. Loreau, "Global relationship between phytoplankton diversity and productivity in the ocean," *Nat. Commun.* **5**, 4299 (2014).
4. T. Platt, "Primary production of the ocean water column as a function of surface light intensity: algorithms for remote sensing," *Deep Sea Res. A* **33**, 149–163 (1986).
5. J. Campbell, D. Antoine, R. Armstrong, K. Arrigo, W. Balch, R. Barber, M. Behrenfeld, R. Bidigare, J. Bishop, M.-E. Carr, W. Esaias, P. Falkowski, N. Hoepffner, R. Iverson, D. Kiefer, S. Lohrenz, J. Marra, A. Morel, J. Ryan, V. Vedernikov, K. Waters, C. Yentsch, and J. Yoder, "Comparison of algorithms for estimating ocean primary production from surface chlorophyll, temperature, and irradiance," *Global Biogeochem. Cycles* **16**, 9-1–9-15 (2002).
6. J. J. Walsh, D. A. Dieterle, and M. B. Meyers, "A simulation analysis of the fate of phytoplankton within the Mid-Atlantic Bight," *Cont. Shelf Res.* **8**, 757–787 (1988).
7. P. G. Falkowski and A. D. Woodhead, *Agricultural and Forest Meteorology* (Plenum, 1992).
8. T. Kameda and J. Ishizaka, "Size-fractionated primary production estimated by a two-phytoplankton community model applicable to ocean color remote sensing," *J. Oceanogr.* **61**, 663–672 (2005).
9. T. J. Smyth, G. H. Tilstone, and S. B. Groom, "Integration of radiative transfer into satellite models of ocean primary production," *J. Geophys. Res.* **110**, 1–11 (2005).
10. I. Asanuma, "Chapter 4: Depth and time resolved primary productivity model examined for optical properties of water," in *Global Climate Change and Response of Carbon Cycle in the Equatorial Pacific and Indian Oceans and Adjacent Landmasses*, Elsevier Oceanography Series (Elsevier, 2007), Vol. **73**, pp. 89–106.
11. K. R. Arrigo, G. L. van Dijken, and S. Bushinsky, "Primary production in the Southern Ocean, 1997–2006," *J. Geophys. Res.* **113**, 1997–2006 (2008).
12. S. Tang, C. Chen, H. Zhan, and T. Zhang, "Determination of ocean primary productivity using support vector machines," *Int. J. Remote Sens.* **29**, 6227–6236 (2008).
13. D. Antoine and A. Morel, "Oceanic primary production: 1. Adaptation of a spectral light-photosynthesis model in view of application to satellite chlorophyll observations," *Global Biogeochem. Cycles* **10**, 43–55 (1996).
14. M. E. Carr, "Estimation of potential productivity in eastern boundary currents using remote sensing," *Deep Sea Res. II* **49**, 59–80 (2001).
15. M. J. Behrenfeld, E. Boss, D. A. Siegel, and D. M. Shea, "Carbon-based ocean productivity and phytoplankton physiology from space," *Global Biogeochem. Cycles* **19**, 1–14 (2005).
16. S. Sathyendranath and T. Platt, "The spectral irradiance field at the surface and in the interior of the ocean: a model for applications in oceanography and remote sensing," *J. Geophys. Res.* **93**, 9270–9280 (1988).
17. C.-C. Liu, "Fast and accurate model of underwater scalar irradiance for stratified Case 2 waters," *Opt. Express* **14**, 1703–1719 (2006).
18. S. Bélanger, M. Babin, and J.-E. Tremblay, "Increasing cloudiness in Arctic damps the increase in phytoplankton primary production due to sea ice receding," *Biogeosciences* **10**, 4087–4101 (2013).
19. C. Gueymard, "An atmospheric transmittance model for the calculation of the clear sky beam, diffuse and global photosynthetically active radiation," *Agric. For. Meteorol.* **45**, 215–229 (1989).

20. R. Pinker and I. Laszlo, "Global distribution of photosynthetically active radiation as observed from satellites," *J. Clim.* **5**, 56–65 (1992).
21. S. Liang, T. Zheng, R. Liu, H. Fang, S.-C. Tsay, and S. Running, "Estimation of incident photosynthetically active radiation from moderate resolution imaging spectrometer data," *J. Geophys. Res.* **111**, 1–13 (2006).
22. T. Zheng, S. Liang, and K. Wang, "Estimation of incident photosynthetically active radiation from GOES visible imagery," *J. Appl. Meteorol. Climatol.* **47**, 853–868 (2008).
23. R. Frouin and B. Chertok, "A technique for global monitoring of net solar irradiance at the ocean surface. Part I: Model," *J. Appl. Meteorol.* **31**, 1056–1066 (1992).
24. J. Laliberté, S. Bélanger, and R. Frouin, "Evaluation of satellite-based algorithms to estimate photosynthetically available radiation (PAR) reaching the ocean surface at high northern latitudes," *Remote Sens. Environ.* **184**, 199–211 (2016).
25. L. Alados-Arboledas, F. J. Olmo, I. Alados, and M. Pérez, "Parametric models to estimate photosynthetically active radiation in Spain," *Agric. For. Meteorol.* **101**, 187–201 (2000).
26. I. Alados, F. J. Olmo, I. Foyo-Moreno, and L. Alados-Arboledas, "Estimation of photosynthetically active radiation under cloudy conditions," *Agric. For. Meteorol.* **102**, 39–50 (2000).
27. R. Frouin, J. McPherson, K. Ueyoshi, and B. A. Franz, "A time series of photosynthetically available radiation at the ocean surface from SeaWiFS and MODIS data," *Proc. SPIE* **8525**, 852519 (2012).
28. Y. Zhang, W. B. Rossow, A. A. Lacis, V. Oinas, and M. I. Mishchenko, "Calculation of radiative fluxes from the surface to top of atmosphere based on ISCCP and other global data sets: refinements of the radiative transfer model and the input data," *J. Geophys. Res.* **109**, 1–27 (2004).
29. R. E. Bird and C. Riordan, "Simple solar spectral model for direct and diffuse irradiance on horizontal and tilted planes at the earth's surface for cloudless atmospheres," *J. Clim. Appl. Meteorol.* **25**, 87–97 (1986).
30. W. W. Gregg and K. L. Carder, "A simple spectral solar irradiance model for cloudless maritime atmospheres," *Limnol. Oceanogr.* **35**, 1657–1675 (1990).
31. F. Kasten and G. Czeplak, "Solar and terrestrial radiation dependent on the amount and type of cloud," *Sol. Energy* **24**, 177–189 (1980).
32. S. Nann and C. Riordan, "Solar spectral irradiance under clear and cloudy skies: measurements and a semiempirical model," *J. Appl. Meteorol.* **30**, 447–462 (1991).
33. D. A. Siegel, T. K. Westberry, and J. C. Ohlmann, "Cloud color and ocean radiant heating," *J. Clim.* **12**, 1101–1116 (1999).
34. P. Ricchiazzi, S. Yang, C. Gautier, and D. Sowle, "SBDART: a research and teaching software tool for plane-parallel radiative transfer in the Earth's atmosphere," *Bull. Am. Meteorol. Soc.* **79**, 2101–2114 (1998).
35. B. Mayer and A. Kylling, "Technical note: the libRadtran software package for radiative transfer calculations—description and examples of use," *Atmos. Chem. Phys. Discuss.* **5**, 1319–1381 (2005).
36. A. Berk, L. S. Bernstein, G. P. Anderson, P. K. Acharya, D. C. Robertson, J. H. Chetwynd, and S. M. Adler-Golden, "MODTRAN cloud and multiple scattering upgrades with application to AVIRIS," *Remote Sens. Environ.* **65**, 367–375 (1998).
37. C. D. Mobley and L. K. Sundman, *Hydrolight 4.2 Users Guide* (Sequoia Scientific, 2001).
38. IOCCG, "Ocean colour remote sensing in polar seas," M. Babin, K. Arrigo, S. Bélanger, and M.-H. Forget, eds., IOCCG Report Series, No. 16 (International Ocean Colour Coordinating Group, 2015).
39. A. Morel and J. M. André, "Pigment distribution and primary production in the western Mediterranean as derived and modeled from coastal zone color scanner observations," *J. Geophys. Res.* **96**, 12685–12698 (1991).
40. F. W. Dobson and S. D. Smith, "Bulk models of solar radiation at sea," *Q. J. R. Meteorol. Soc.* **114**, 165–182 (1988).
41. M. I. Budyko, *Climate and Life*, International Geophysics (Academic, 1974).
42. V. S. Saba, M. A. M. Friedrichs, D. Antoine, R. A. Armstrong, I. Asanuma, M. J. Behrenfeld, A. M. Ciotti, M. Dowell, N. Hoepffner, K. J. W. Hyde, J. Ishizaka, T. Kameda, J. Marra, F. Melin, A. Morel, J. O'Reilly, M. Scardi, W. O. Smith, T. J. Smyth, S. Tang, J. Uitz, K. Waters, and T. K. Westberry, "An evaluation of ocean color model estimates of marine primary productivity in coastal and pelagic regions across the globe," *Biogeosciences* **8**, 489–503 (2011).
43. D. Antoine, F. D'Ortenzio, S. B. Hooker, G. Béchu, B. Gentili, D. Tailliez, and A. Scott, "Assessment of uncertainty in the ocean reflectance determined by three satellite ocean color sensors (MERIS, SeaWiFS, MODIS) at an offshore site in the Mediterranean Sea (BOUSSOLE project)," *J. Geophys. Res.* **113**, C07013 (2008).
44. R. Frouin, B. Franz, and M. Wang, "Algorithm to estimate PAR from SeaWiFS data Version 1.2-Documentation," NASA Tech Memo 206892 (2003), pp. 46–50.
45. R. E. Payne, "Albedo of the sea surface," *J. Atmos. Sci.* **29**, 959–970 (1972).
46. J. H. Pierluissi and G.-S. Peng, "New molecular transmission band models for LOWTRAN," *Opt. Eng.* **24**, 541–547 (1985).
47. W. J. Wiscombe and J. W. Evans, "Exponential-sum fitting of radiative transmission functions," *J. Comput. Phys.* **24**, 416–444 (1977).
48. K. Stamnes, S. C. Tsay, W. Wiscombe, and K. Jayaweera, "Numerically stable algorithm for discrete-ordinate-method radiative transfer in multiple scattering and emitting layered media," *Appl. Opt.* **27**, 2502–2509 (1988).
49. R. A. McClatchey, W. Fenn, J. E. A. Selby, F. E. Volz, and J. S. Garing, "Optical properties of the atmosphere," AFCRL-710279 (Air Force Cambridge Research Laboratories, 1971), p. 88.
50. Y. J. Lee, P. A. Matrai, M. A. M. Friedrichs, V. S. Saba, D. Antoine, M. Ardyna, I. Asanuma, M. Babin, S. Belanger, M. Benoit-Gagne, E. Devred, M. Fernandez-Mendez, B. Gentili, T. Hirawake, S. H. Kang, T. Kameda, C. Katilein, S. H. Lee, Z. Lee, F. Melin, M. Scardi, T. J. Smyth, S. Tang, K. R. Turpie, K. J. Waters, and T. K. Westberry, "An assessment of phytoplankton primary productivity in the Arctic Ocean from satellite ocean color/in situ chlorophyll-a based models," *J. Geophys. Res.* **120**, 6508–6541 (2015).
51. K. R. Arrigo, D. L. Worthen, A. Schnell, and M. P. Lizotte, "Primary production in southern ocean waters," *J. Geophys. Res.* **103**, 15587–15600 (1998).
52. S. C. Doney, I. Lima, J. K. Moore, K. Lindsay, M. J. Behrenfeld, T. K. Westberry, N. Mahowald, D. M. Glover, and T. Takahashi, "Skill metrics for confronting global upper ocean ecosystem-biogeochemistry models against field and remote sensing data," *J. Mar. Syst.* **76**, 95–112 (2009).
53. M. A. M. Friedrichs, M. E. Carr, R. T. Barber, M. Scardi, D. Antoine, R. A. Armstrong, I. Asanuma, M. J. Behrenfeld, E. T. Buitenhuis, F. Chai, J. R. Christian, A. M. Ciotti, S. C. Doney, M. Dowell, J. Dunne, B. Gentili, W. Gregg, N. Hoepffner, J. Ishizaka, T. Kameda, I. Lima, J. Marra, F. Melin, J. K. Moore, A. Morel, R. T. O'Malley, J. O'Reilly, V. S. Saba, M. Schmeltz, T. J. Smyth, J. Tjiputra, K. Waters, T. K. Westberry, and A. Winguth, "Assessing the uncertainties of model estimates of primary productivity in the tropical Pacific Ocean," *J. Mar. Syst.* **76**, 113–133 (2009).
54. A. J. Schweiger, R. W. Lindsay, J. R. Key, and J. A. Francis, "Arctic clouds in multiyear satellite data sets," *Geophys. Res. Lett.* **26**, 1845–1848 (1999).
55. R. J. W. Brewin, S. Sathyendranath, D. Müller, C. Brockmann, P. Y. Deschamps, E. Devred, R. Doerffer, N. Fomferra, B. Franz, M. Grant, S. Groom, A. Horsemann, C. Hu, H. Krasemann, Z. Lee, S. Maritorena, F. Melin, M. Peters, T. Platt, P. Regner, T. Smyth, F. Steinmetz, J. Swinton, J. Werrell, and G. N. White, "The ocean colour climate change initiative: III. A round-robin comparison on in-water bio-optical algorithms," *Remote Sens. Environ.* **162**, 271–294 (2015).
56. J. Cohen and P. Cohen, *Applied Multiple Regression/Correlation Analysis for the Behavioral Sciences* (L. Erlbaum Associates, 1983).
57. D. Ramon, D. Jolivet, and J. Tan, "Estimating photosynthetically available radiation at the ocean surface for primary production (3P Project): modeling, evaluation, and application to global MERIS," *Proc. SPIE* **9878**, 98780D (2016).
58. K. B. Bishop, B. Rossow, and G. Dutton, "Surface solar irradiance from the International Satellite Cloud Climatology Project 1983–1991," *J. Geophys. Res.* **102**, 6883–6910 (1997).
59. S. Zeng, C. Cornet, F. Parol, J. Riedi, and F. Thieuleux, "A better understanding of cloud optical thickness derived from the passive sensors MODIS/AQUA and POLDER/PARASOL in the A-Train constellation," *Atmos. Chem. Phys.* **12**, 11245–11259 (2012).

60. W. Tang, J. Qin, K. Yang, S. Liu, N. Lu, and X. Niu, "Retrieving high-resolution surface solar radiation with cloud parameters derived by combining MODIS and MTSAT data," *Atmos. Chem. Phys.* **16**, 2543–2557 (2016).
61. K. R. Arrigo and G. L. van Dijken, "Phytoplankton dynamics within 37 Antarctic coastal polynya systems," *J. Geophys. Res.* **108**, 3271 (2003).
62. K. R. Arrigo, G. L. van Dijken, and S. Bushinsky, "Primary production in the Southern Ocean, 1997-2006," *J. Geophys. Res.* **113**, C08004 (2008).
63. S. Pabi, G. L. van Dijken, and K. R. Arrigo, "Primary production in the Arctic Ocean, 1998-2006," *J. Geophys. Res.* **113**, C08005 (2008).
64. K. R. Arrigo and G. L. van Dijken, "Secular trends in Arctic Ocean net primary production," *J. Geophys. Res.* **116**, C09011 (2011).
65. K. R. Arrigo, G. L. van Dijken, and A. L. Strong, "Environmental controls of marine productivity hot spots around Antarctica," *J. Geophys. Res.* **120**, 5545–5565 (2015).
66. R. Frouin, D. Ramon, E. Boss, D. Jolivet, M. Compiégne, J. Tan, H. Bouman, T. Jackson, B. Franz, T. Platt, and S. Sathyendranath, "Satellite radiation products for ocean biology and biogeochemistry: needs, state-of-the-art, gaps, development priorities, and opportunities," *Front. Mar. Sci.* **5**, 3 (2018).